

Contents lists available at ScienceDirect

Transportation Research Part C

journal homepage: www.elsevier.com/locate/trc



On multi-class automated vehicles: Car-following behavior and its implications for traffic dynamics*



Wissam Kontar ^a, Tienan Li ^b, Anupam Srivastava ^a, Yang Zhou ^a, Danjue Chen ^b, Soyoung Ahn ^{a,*}

- ^a Civil and Environmental Engineering, University of Wisconsin-Madison, United States
- ^b Civil and Environmental Engineering, University of Massachusetts, Lowell, United States

ARTICLE INFO

Keywords: Car-following Linear Control Model Predictive Control Convolved Gaussian Process Heterogeneous CAVs Traffic Dynamics

ABSTRACT

This paper develops a unifying framework to unveil the physical car-following (CF) behaviors of automated vehicles (AVs) under different control paradigms and parameter settings. The proposed framework adopts the flexible asymmetric behavior (AB) model to reveal the control mechanisms and their manifestation in the physical CF behavior, particularly their response to traffic disturbances. A mapping relationship between the AB model parameters and control parameters is then obtained to understand the range of CF behavior possible. Finally, a predictive modeling approach based on a logistic classifier coupled with a convoluted Multivariate Gaussian Process (MSP) is designed to predict the CF behavior of an AV. Analysis of two well-known controllers, linear state-feedback and Model Predictive Control (MPC), show how the proposed framework can uncover the CF mechanisms and provide insights into traffic-level disturbance evolution. The proposed analysis framework remains scalable and can be applied to a variety of controllers. Ultimately, it can guide AV control design that is not myopic, but considers traffic-level performance.

1. Introduction

Advancements in Automated vehicle (AV) technologies have given rise to various vehicle control paradigms. These advancements set the stage for a new era of traffic flow system, which will be characterized by heterogeneity and complex dynamics. The current literature on traffic heterogeneity is dedicated to differences in vehicle types, preference and behavior of human drivers, and more recently, mixed traffic (consisting of human driven vehicles (HDVs) and AVs). However, the introduction of different control paradigms and different parameter settings within each, will add a new dimension of heterogeneity; one that comes from AVs themselves. We conjecture that different AV controllers will respond differently to car-following (CF) disturbances (e.g., deceleration followed by acceleration), and that can translate into a major impact on traffic dynamics. Thus, exploring a range of CF behavior of multi-class AVs (due to different control paradigms and settings) will pave the way towards understanding their traffic impacts and developing control strategies to realize desired traffic performance.

In general, existing control algorithms can be categorized into three main paradigms; (i) linear state-feedback control (Morbidi

E-mail address: sue.ahn@wisc.edu (S. Ahn).

[★] This article belongs to the Virtual Special Issue on IG005584: VSI:ISTTT24.

^{*} Corresponding author.

et al., 2013; Naus et al., 2010; Peppard, 1974; Swaroop et al., 1994; Swaroop and Hedrick, 1996; Talebpour and Mahmassani, 2016), (ii) optimization-based control (Gong et al., 2016; Ma et al., 2017; Zhou et al., 2019; Hoogendoorn et al., 2012; Wang et al., 2014; Chen et al., 2018), and (iii) data driven or artificial intelligence (AI)-based control (Gao and Jiang, 2017; Gao et al., 2016; Hou and Wang, 2013; Hou et al., 2007). Each control paradigm brings unique advantages and challenges in terms of performance, guarantee of stability, and constraint handling. Notably, the linear state-feedback control algorithm has been widely adopted in the literature and field-tested due to its desirable analytical and performance features (Milanés et al., 2013; Shladover et al., 2012; Liu et al., 2018; Van Arem et al., 2006; Zhou et al., 2020; Morbidi and Mariottini, 2012; Öncü et al., 2014). Particularly, it provides a closed formulation for the acceleration of an AV to regulate the deviations of vehicle state from a predefined equilibrium state. The algorithm requires low computational needs and can guarantee both local stability (disturbance dissipation over time) and string stability (disturbance attenuation through a vehicular string) through proper tuning of control parameters. Thus, this method is particularly popular for Adaptive Cruise Control (ACC) and its various forms (Öncü et al., 2014; Petrillo et al., 2018; Qin and Orosz, 2017; Shladover et al., 2015; Marsden et al., 2001; Darbha and Rajagopal, 1999; VanderWerf et al., 2001). However, it lacks a convenient platform to explicitly set constraints or control objectives.

On the contrary, MPC-based vehicle control, a popular method in the optimization-based control paradigm, provides an explicit framework to formulate an objective function and constraints to enable an optimal strategy with prediction capabilities (Zhou et al., 2019; Wang et al., 2014; Zhou et al., 2017b). Specifically, the vehicle's acceleration can be controlled through an optimization function that considers multiple criteria (e.g., control performance, driving comfort, fuel efficiency), while incorporating physical constraints (e.g., upper/lower acceleration bounds, collision-free driving). Notably, MPC adopts a rolling horizon framework, where the optimal acceleration is determined by optimizing the performance predicted over a future time horizon based on the current system measurements and dynamics. Yet, an important limitation of MPC-based vehicle control is the lack of stability guarantees. Some recent work tried to alleviate this limitation (Gong et al., 2016; Gong and Du, 2018; Dunbar and Caveney, 2011; Zhou et al., 2019).

Limited research exists on AI-based, data-driven vehicle control although some studies suggest that AI-based controllers can be more adept at capturing complex vehicular dynamics and tackling complicated driving task compared to the traditional model-based approaches (Lefèvre et al., 2016; Kuderer et al., 2015). Wu et al. (2017) is a notable study that used reinforcement learning to learn how to control AVs in mixed traffic in different scenarios (e.g., stop-and-go traffic, lane-drop, and intersections). However, the performance often depends on its training data and short-term prediction capabilities (Zhou et al., 2017a).

Multiple AV classes stemming from different control paradigms, algorithms, and parameter settings will result in heterogeneous traffic, adding further complexity to traffic dynamics. Note that the heterogeneity in AVs is systematically different from that in HDVs. Heterogeneity in HDVs largely stems from the variability in vehicle types, vehicle characteristics, and driver behavior. In addition to these elements, heterogeneity in AVs has a new dimension: the variability in the control logic and parameter settings. For instance, in linear control, different control gains settings will result in different deceleration-acceleration behavior in response to disturbances. In MPC-based control, multiple objectives are considered, and their weight matrix setting will lead to different driving behavior. Furthermore, in AVs, heterogeneity in drivers can be manifested in some parameter settings. For instance, in many commercial ACC systems, drivers can choose their desired headway preference (time-gap parameter). As the technology develops, it is expected that other parameters, such as maximum acceleration, can also be explicitly customized by users (Talebpour et al., 2011). All these will contribute to heterogeneity within AVs and can produce profound impacts on traffic dynamics.

This paper is interested in how such heterogeneous AV traffic will behave when perturbed by traffic disturbances. Indeed, traffic disturbances are ubiquitous, attributed to instability in CF and lane-changes. Many studies have shown that in pure HDV traffic, such disturbances can instigate congestion and stop-and-go oscillations that grow over space, undermining traffic flow throughput and stability (Chen et al., 2014; Knoop et al., 2009). The disturbance growth is linked to time-varying driver response (e.g., response time) (Chen et al., 2014). While a wealth of studies exist on this subject for HDV traffic, literature on disturbance evolution in heterogeneous and mixed traffic of AVs and HDVs is sparse. As a notable exception, Chen et al. (2019) studied the evolution of traffic void caused by a single disturbance in a heterogeneous system involving AVs and HDVs. In that paper, heterogeneity was manifested in the preferred acceleration rate, desired speed, and CF behavior due to different control objectives (control efficient vehicles and smooth driving vehicles). It was found that such heterogeneity can diminish traffic throughout by creating extra space voids and change traffic properties. While analytical in its approach, the study largely examined simple hypothetical cases (e.g., binary settings of acceleration, desired speed, and AV CF control). Furthermore, a single controller (linear controller) was used in the study. Thus, the current literature lacks a systematic study of heterogeneous AV behavior and their influence on traffic dynamics.

This study aims to better understand the CF behaviors of different classes of AVs and their impacts on traffic dynamics. For tractability, connectivity is not considered in this study. Specifically, the objectives are to (i) characterize the CF behavior of AVs under different control paradigms (i.e., linear control and MPC-based control) and control parameter settings, (ii) investigate discernible differences in the CF behavior among different classes of AVs, and (iii) elucidate how they impact traffic dynamics, particularly disturbance evolution. We seek to gain insights into the physical control mechanisms and how they govern the CF behavior and thus disturbance evolution. Toward this end, we adopt the principles of the physics-based asymmetric behavior (AB) CF model (Laval and Leclercq, 2010; Chen et al., 2012b) to capture key physical features of different control paradigms in a unifying fashion and gain direct insights into disturbance evolution. The use of the AB model is substantiated through an empirical analysis of real AV behavior in two field experiments. Then we analyze the physical control mechanisms of how linear and MPC-based controllers govern the CF behavior; i.e., how control parameter settings translate to the physical CF parameters of the AB model. Furthermore, we map control parameters into the AB model parameters to reveal systematic patterns. Building on this analysis, we formulate a data-driven prediction method based on a logistical classifier coupled with a convoluted Multivariate Gaussian Prediction (MGP) model to predict the AB model parameters given a control parameter setting and disturbance characteristics (i.e., lead vehicle behavior). Based on these results, we

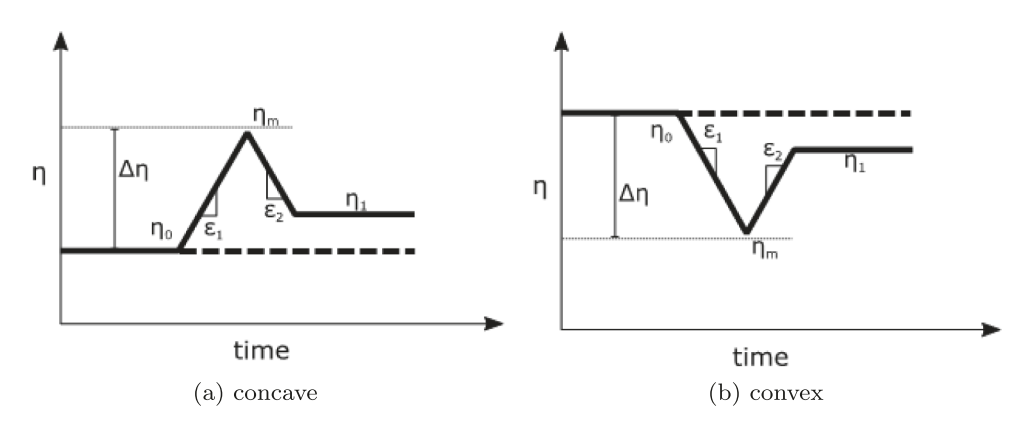


Fig. 1. Reaction pattern, $\eta(t)$, under disturbance.

examine how heterogeneous parameter settings can impact disturbance evolution to elucidate traffic-level behavior via numerical simulations.

Note that originated from control theory and artificial-intelligence fields, most AV control algorithms (including the ones investigated here) naturally lack direct physical insights necessary to understand traffic-level behavior (disturbance amplitude and duration). The microscopic nature of AV control makes it difficult to translate their control mechanisms into traffic-level dynamics. The present research fills this gap by developing an analysis framework to unveil the physical behavior of well-known controllers, in ways that are relatable to the traffic science community. This analysis framework can be applied to a wide variety of controllers, beyond the ones examined in this study. Ultimately, these insights can guide how AV control should be designed with traffic-level performance in mind. Note that some existing string stability concept does provide some useful insights for traffic-level performance. However, it is not enough to explain various aspects of disturbance evolution (e.g., recovery time). Furthermore, stability analysis has been possible (so far) only for linear/linearized controllers and has not crossed the boundaries of other control paradigms. The approach we present, though not capturing all the intricate details of controllers, is able to analyze controllers of different paradigms through the same lens, enabling a more comprehensive look at heterogeneous AV traffic.

The rest of the paper is organized as follows: Section 2 presents an empirical analysis of real AV data from two field experiments, using the AB model. Sections 3 and 4 entail a detailed analysis of a linear controller and a MPC-based controller, respectively, including control mechanisms and their relations to CF behavior and disturbance propagation. The data-driven prediction method to predict the AV CF behavior is presented in Section 5. Section 6 provides insights into the traffic-level implications. Finally, discussion and concluding remarks are provided in Section 7.

2. The Asymmetric Behavioral (AB) Model for AVs

This section will introduce the AB model and substantiate its use as a flexible and unifying framework for AV CF behavior analysis. Through an empirical analysis of two field experimental data sets, we show that the AB model can capture different AV CF behaviors due to different control logic and physical mechanisms for disturbance evolution.

2.1. The AB Model Formulation

In this study, we adopt the physics-based AB CF model Chen et al. (2012a), an extended model of Newell's simplified CF model Newell (2002), for two main reasons: (i) Due to its flexibility in capturing different CF behaviors around disturbances, it can serve as a unifying framework to analyze different paradigms of AV control; (ii) Its parsimonious framework can capture key physical CF characteristics that can be explicitly connected to traffic-level impact, particularly disturbance evolution. Below is a summary of the AB model, building on Newell's simplified CF model.

Newell's simplified CF model (Newell, 2002) describes that a vehicle maintains a *constant* minimum spacing, δ , and time gap (driver response time), τ , with respect to its leader under congested conditions. This means that the follower behaves the same as its leader along constant traffic waves, w, and thus a disturbance, marked by a cycle of deceleration-acceleration, does not grow nor decay. The AB model extends this framework by incorporating the deviation from Newell's model through an additional parameter, $\eta(t)$. This parameter prescribes the vehicle's temporal deviation in τ or δ from its *equilibrium* position defined by Newell's model. The underlying mathematical formulation is presented in Eq. (4)

$$y_i(t) = y_{i-1}(t - \eta_i(t)\tau) - \eta_i(t)\delta$$
 (1)

where y_i and y_{i-1} are the positions of vehicle i and its leader i-1, respectively. Note that the AB model describes the vehicle behavior only when constrained by the preceding vehicle. The evolution of $\eta(t)$ reveals the driver's CF characteristics. When a driver experiences a disturbance, η is found to exhibit several evolutionary shapes, named the *reaction pattern*, including concave and convex reaction patterns as illustrated in Fig. 1. A concave (convex) pattern suggests that a vehicle initially lags behind (leads ahead of) the equilibrium

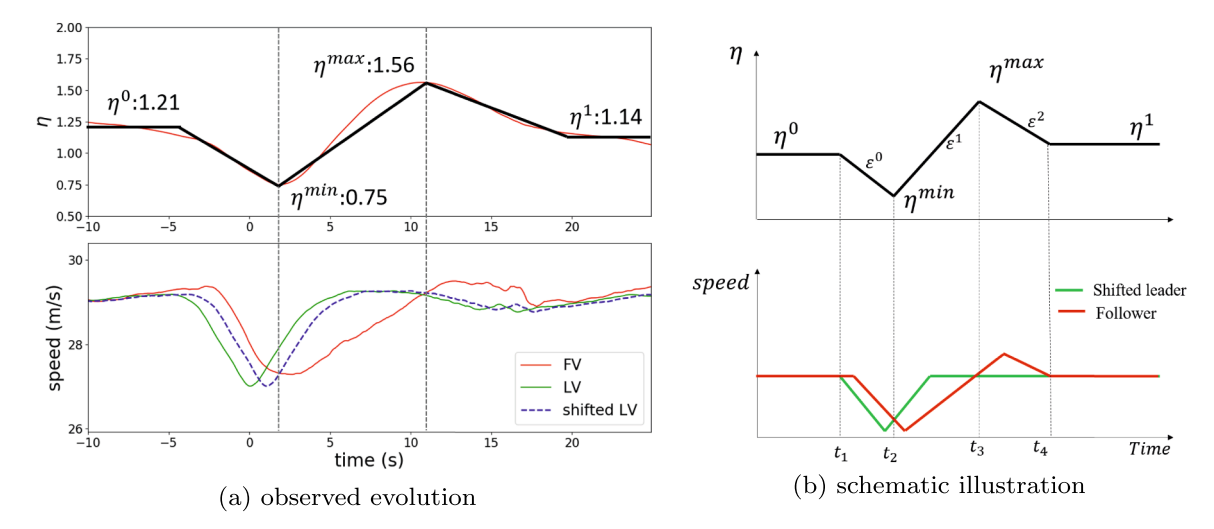


Fig. 2. η evolution, $\eta(t)$, from MA experiment.

position (as defined by Newell's model and noted as dashed lines in 1) and then gradually recovers.

Note that while the reaction pattern does not capture all the minutiae of vehicle trajectory, it highlights the key aggregate characteristics and trends that influence disturbance evolution (e.g., magnitude, path and duration of different disturbance phases). Particularly, the reaction pattern can provide a direct insight into disturbance evolution as it describes the vehicle position over time relative to the 'neutral' position (where disturbances do not grow or decay) according to Newell's model. Furthermore, the reaction pattern can take any shapes, lending the model flexibility to analyze the CF behaviors under different AV controllers. Notably, a single pattern (e.g., either concave or convex) for each vehicle was envisioned in the original AB model framework. As we will show, however, composite patterns (e.g., concave followed by convex) are observed for well-known AV controllers, as well as real AVs (with ACC function) on the road. These patterns are physically linked to disturbance amplification or decay, and duration.

2.2. Empirical Analysis of AV CF Behavior using the AB Model

In this subsection, we present an empirical analysis of CF behavior of ACC vehicles to demonstrate the effectiveness of using the AB model framework. We use data from two field experiments involving different types of AVs, one conducted by the authors and one conducted by Stern et al. (2018), referred to as "Arizona Control Experiment".

2.2.1. MA Control Experiment

Recently, we have conducted experiments using a commercial car model equipped with ACC in Lowell, MA. Below we provide a brief introduction and the details can be found in Li et al. (2021). Specifically, we have conducted two-vehicle CF experiments, in which the leader is a HDV and the follower is the ACC vehicle. The leader was instructed to cruise at a speed around $29 \, m/s$, decelerate to a lower speed in the range of $25-27 \, m/s$ (varied by different cases), and then accelerate back to $29 \, m/s$. The ACC was active in the whole process.

While the controller is unknown due to the proprietary right, our field data suggest that it is likely a linear controller (as supported by our calibration outcome to be provided in Section 5.4). Particularly, the ACC behavior is evidently "reactive". Fig. 2 shows one example speed profile and the corresponding η evolution of the ACC, which shows a convex-concave reaction pattern (red plot for actual data and black for approximation). Note that here the η is measured based on the δ ratio, assuming a constant time gap. More details will be provided in the following section.

To explain this result, we use a schematic illustration in Fig. 2b. The ACC follower initially travels at the same stable speed as the leader. Then the leader conducts a deceleration-acceleration cycle. The ACC vehicle reacts to the leader's deceleration with a delay before it decelerates. Because of the delay, η decreases from η^0 and it reaches the minimum η^{min} when the speed of the ACC equals to the leader; see the (t_1, t_2) period. After that, η starts to increase; see the (t_2, t_3) period. When the leader resumes the desired speed, the ACC vehicle is still accelerating to catch up with the leader. Therefore, η^{max} occurs at t_3 when the speed of the ACC vehicle equals to the leader's. At this time, the ACC vehicle has not closed the extra gap ahead (i.e., η^{max} is much larger than η^0 , which is often the case in our experiment). Thus, the ACC vehicle accelerates beyond the desired speed to close the gap and then decelerates to resume the desired speed; see (t_3, t_4) .

2.2.2. Arizona Control Experiments

A recent study Stern et al. (2018) has conducted a set of experiments in Arizona to demonstrate that one Connected AV (CAV) can effectively resolve stop-and-go oscillations. The experiments used a ring road setting with 21 –22 vehicles including one CAV. There were three experiments (A, B, and C), but we exclude experiment B as there was only one run. Experiments A and C adopted different

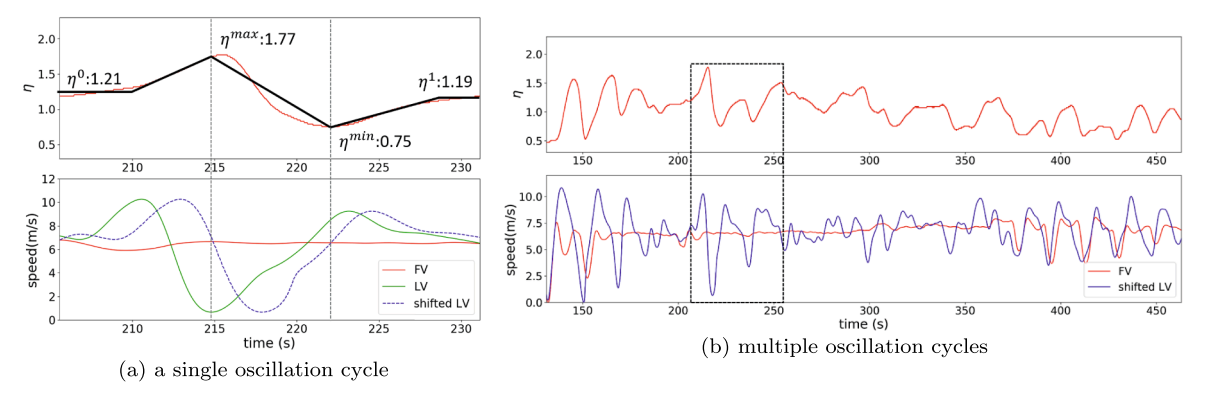


Fig. 3. η evolution, $\eta(t)$, of the CAV in Arizona experiment (experiment A).

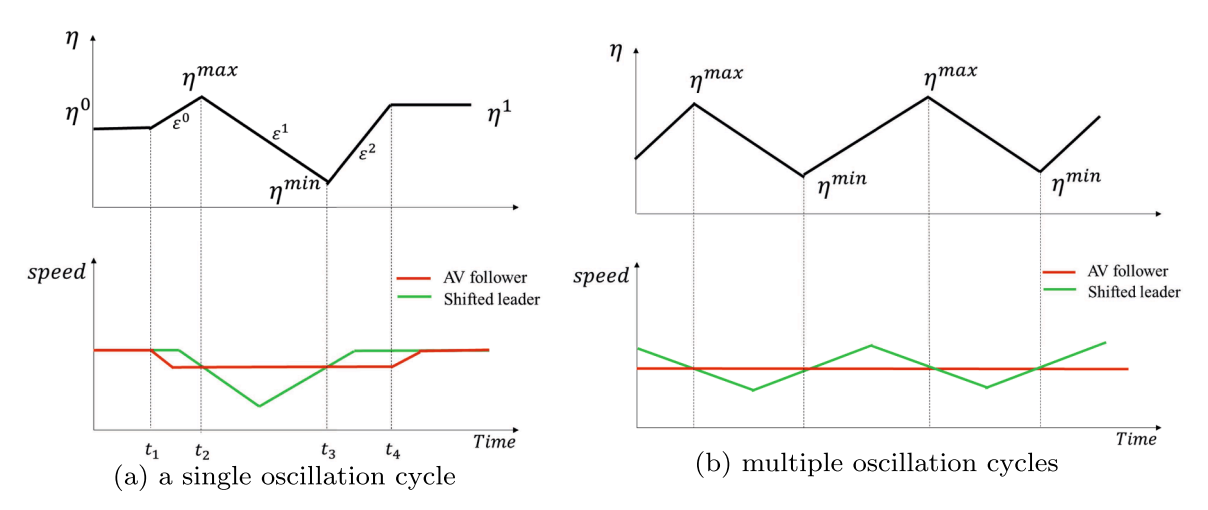


Fig. 4. Schematic illustration of η evolution.

controllers. The controller for experiment A required the CAV to maintain the desired speed when possible or a lower speed per safety requirement (determined by the research team). The controller for experiment C had a similar principle, except that the speed of the CAV was determined based on the average speed of the vehicle in front.

Note that the control in these experiments is different from the conventional CF controller design. It was more "proactive" (different from the "reactive" manner of the MA experiments) in the sense that anticipating an oscillation the CAV was controlled to drive at a lower speed during the acceleration phase, such that it was able to maintain that speed during a deceleration phase, thereby ending a stop-and-go cycle.

The results of the η evolution show consistent patterns in the two experiments. Note that to measure the η values, we used the wave speeds of -9.15m/s and -9.25m/s for the two experiments, estimated from the data. Specifically, Fig. 3a shows a segment with a single oscillation cycle, and Fig. 3b shows the η evolution with multiple continuous oscillations. The reaction pattern in the single-oscillation case exhibits a concave-convex shape (red plot for actual data and black for approximation), while the evolution is more complex in the multi-oscillation case.

To explain these results, we provide a schematic illustration. In Fig. 4, we illustrate the speed evolution and the resulting η profile in the single-oscillation case.

Per the control principle, the speed of the CAV will be pre-set to a lower speed than the leader and then remains at that level until the oscillation ends, afterwards the CAV will accelerate to catch up with the leader. As a result, η first increases from the initial equilibrium level η^0 . The increase continues until the speed of the CAV equals to the leader's; see the time period of (t_1, t_2) . Once the leader's speed dips below the CAV's cruising speed, η starts to decrease until the leader's speed once again exceeds the CAV's cruising speed and η^{min} is achieved. After that, η increases from η^{min} to a new stable value, η^1 , when the two vehicles reach the same speed. If oscillations occur continuously without stable periods, the CAV will need to maintain the low speed through multiple cycles. In this case, the η evolution is absent of stable periods; see Fig. 4b for an illustration. This is also reflected in the empirical data in Fig. 3b, particularly in the period labeled. Similar patterns are observed for experiment C. Overall, it is found that the CAV behavior designed to "proactively" manage stop-and-go cycles can be effectively captured by the AB model.

The empirical observations from the MA and Arizona experiments show that the reaction pattern can vary with the controller design. However, it can consistently and effectively capture the main characteristics of the controllers and explain the governing physical behavior for each controller. In the following sections, we investigate using the AB model two well-known AV controllers, linear and MPC-based controllers, particularly how the control parameter setting governs the reaction pattern, physical CF behavior, and disturbance evolution. Details follow.

3. Analysis of Linear Controller

This section briefly introduces a typical linear controller and analyzes its CF behavior. Specifically, we show how the control parameter setting translates into the $\eta(t)$ profile of the AB model, including the shape (convex, concave), η^{min} , and η^{max} , to gain insight into the range of CF behavior possible and its impact on disturbance evolution.

3.1. Controller Background

Linear controller is a highly adopted control algorithm due to its desirable analytical properties (closed-form formulation) and stable performance. This control strategy has seen significant promise in real life application on ACC/CACC systems (Shladover et al., 2015) with a rich theoretical/methodological literature as well as some field testing experiments (Milanés and Shladover, 2014; Zhou et al., 2020; Morbidi et al., 2013; Naus et al., 2010). While various linear controllers exist in the literature, the underlying control strategy is fairly consistent. In this paper, we base our analysis on the state-of-the-art linear controller designed by Zhou and Ahn (2019). This controller provides robust car-following control by considering uncertainties in vehicle dynamics. To keep the scope reasonable and tractable, we assume an ACC system without communication.

The adopted linear controller follows a hierarchical control scheme consisting of lower-level and upper-level controllers, working in conjunction to regulate the vehicle's acceleration. The upper-level controller regulates the AV's acceleration to follow a pre-defined equilibrium spacing, while the lower-level controller determines the realized acceleration after accounting for vehicle dynamics. The upper-level controller follows the constant time-gap policy Swaroop et al. (1994) that models the equilibrium spacing as shown in Eq. (4)

$$d_i^*(t) = v_i(t) \times \tau_i^* + \delta_i^* \tag{2}$$

where $d_i^*(t)$ is the desired equilibrium spacing of vehicle i at any time t; $v_i(t)$ is the respective speed of vehicle i; τ_i^* is the constant time gap (set to 1 s); and δ_i^* is the standstill distance. Accordingly, the deviation from the equilibrium spacing can be written as $\Delta d_i(t) = d_i(t) - d_i^*(t)$, where $d_i(t)$ represents the actual spacing between vehicle i and its leader (i-1) at time t, and the speed difference between vehicle i and its leader (i-1) is $\Delta v_i(t) = v_{i-1}(t) - v_i(t)$.

The lower-level design uses the general longitudinal vehicle dynamics (GLVD) equation to incorporate vehicle dynamics due to aerodynamic drag, road gradient, vehicle condition, gear position, etc. Yi and Do Kwon (2001). In Zhou and Ahn (2019), vehicle dynamics is modeled with the first-order approximation as in Wang (2018), as shown below:

$$\dot{a}_i(t) = \frac{-1}{T_{i,L}} a_i(t) + \frac{K_{i,L}}{T_{i,L}} u_i(t) \tag{3}$$

where $\dot{a}_i(t)$ is the jerk; $a_i(t)$ is the realized acceleration; $T_{i,L}$ is the actuation lag; $K_{i,L}$ is the ratio between demanded and realized acceleration (typically taken as 1); and $u_i(t)$ is the final demanded acceleration from the controller.

The state-space system is formulated according to a system state described by $x_i(t) = [\Delta d_i(t), \Delta v_i(t), a_i(t)]^T$ and input state as $u_i(t)$. Accordingly, Eqs. 2, 3 are formulated as a linear time invariant system (LTI) as:

$$\dot{x}_i(t) = A_i x_i(t) + B_i u_i(t) + Da_{i-1}(t) \tag{4}$$

$$\text{with } A_i(t) = \begin{bmatrix} 0 & 1 & -\tau_i^* \\ 0 & 0 & -1 \\ 0 & 0 & \frac{-1}{T_{i,L}} \end{bmatrix}, B_i(t) = \begin{bmatrix} 0 \\ 0 \\ K_{i,L} \\ T_{i,L} \end{bmatrix}, D = \begin{bmatrix} 0 \\ 1 \\ 0 \end{bmatrix}.$$

Adopting the widely-used linear control law Stankovic et al. (2000); Van Arem et al. (2006) in a decentralized fashion, the desired acceleration of vehicle i at time t, $u_i(t)$, is determined in a feedback fashion by measuring $x_i(t)$ from vehicle sensors, as follows:

$$u_{i}(t) = K_{i}^{T} x_{i}(t) + K_{fi} a_{i-1}(t - \theta)$$

$$K_{i}^{T} = [k_{si}, k_{vi}, k_{ai}]$$
(5)

where k_{si}, k_{vi}, k_{ai} are the feedback gains for the deviation from equilibrium spacing ($\Delta d_i(t)$), speed difference ($\Delta v_i(t)$) and acceleration ($a_i(t)$), respectively. Note that K_{fi} (feedforward gain) and θ (communication delay) are both set to zero for the ACC system.

One can clearly note from Eqn. (5) the inherent relation between the feedback gains (K_i^T) and the CF behavior of the controlled vehicle as they are directly related to deviations from the desired state. The parameter setting of K_i^T denotes the regulation magnitude

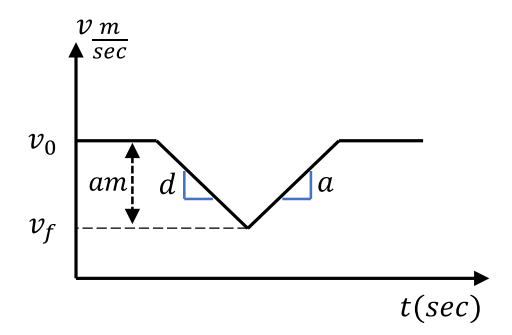


Fig. 5. Designed velocity profile for lead vehicle.

Table 1Default parameter settings for simulation setup of linear controller.

Parameter	Value
$T_{i,L}$	0.3 s
$K_{i,L}$	1
t_s	0.01 s
$ au^*$	1 s
δ^*	5 m

for each component in the system state $x_i(t)$. Thus, to study the impacts of K_i^T , we perform numerical simulations to generate vehicle trajectories based on the above linear controller with different K_i^T settings and then map K_i^T gains to the shape of $\eta(t)$ and the related parameters to give direct insights into how different control gains govern CF behavior individually and collectively.

3.2. Numerical Simulation Setup

Even though the linear controller adopted in this study has a closed-form expression, it is challenging to draw physical insights analytically due to three control gains working together dynamically. Thus, we take a numerical approach: we perform systematic numerical simulations to generate AV trajectories in a variety of settings and analyze the trajectories using the AB framework to derive physical insights.

Our simulations are based on a set of leader trajectories, pre-designed to mimic HDV behavior during a single cycle of oscillations, as seen in Fig. 5. A total of 35 different leading trajectories were designed with varying deceleration (d), acceleration (a), and oscillation amplitude (am) values, while the initial velocity (v_0) was fixed at 30m/sec. For realistic trajectories, we chose the d and a values within $[-6m/sec^2, +6m/sec^2]$ based on the observations in the filtered NGISM data Montanino and Punzo (2013). We adopt a latin hypercube sampling procedure Stein (1987) to draw different combinations of d and a. Similarly, we sampled the oscillation amplitude within [3m/sec, 27m/sec]. For the control gains, K_i^T , we design a large space of gain values that span beyond the feasible regions for stability in Zhou and Ahn (2019), totalling 216,000 (i.e., 60^3) different combinations. Specifically, k_s (we drop the index i for general reference) and k_v range within [0.05,3], and k_a within [-2.95,0], with a constant increment to obtain 60 samples for each. This setting allows us to gain insights into the range of CF behavior possible and provide a rich data set for our prediction models in Section 6.

The simulated trajectories are then analyzed to compute $\eta(t)$ and extract the model parameters, η^{min} , η^{max} . In computing $\eta(t)$, information/wave speed is a necessary parameter. For the linear controller, this is tricky. The linear controller, as seen earlier, has three state space variables: deviation from desired spacing, speed difference with leader, and acceleration of vehicle. For the latter two, information of any change is available to the follower in the next control time step for reaction. However, information regarding any change in deviation from desired spacing is effectively lagged by τ^* (a follower always maintaining perfect desired spacing would result in a follower trajectory reflecting Newell's model with τ^* time gap, see Eqn. (2). Thus, the overall information travel time (or speed) depends on both the gain settings and the state space conditions, and is impossible to calculate precisely. Instead we pick the slowest of the three, τ^* , and use a variation of Eqn. (1) with fixed time gap (i.e., $\eta_t(t)\tau=\tau^*$) but varying spacing $\eta_s(t)^*$ δ^* to compute $\eta(t)\equiv\eta_s(t)$, as shown in Eqn. (7). Other default parameter setting for simulation is shown in Table 1. Note that for conciseness, we present analysis results for a single leader trajectory: $d=-3m/sec^2$, $a=1.5m/sec^2$, and a=27m/sec. The findings from all other studied trajectories are consistent with the discussions provided below. Note that, moving forward we will drop the subscript s and use $\eta_s(t)$ as $\eta(t)$.

$$y_i(t) = y_{i-1}(t - \eta_t(t)\tau) - \eta_s(t)\delta$$
(6)

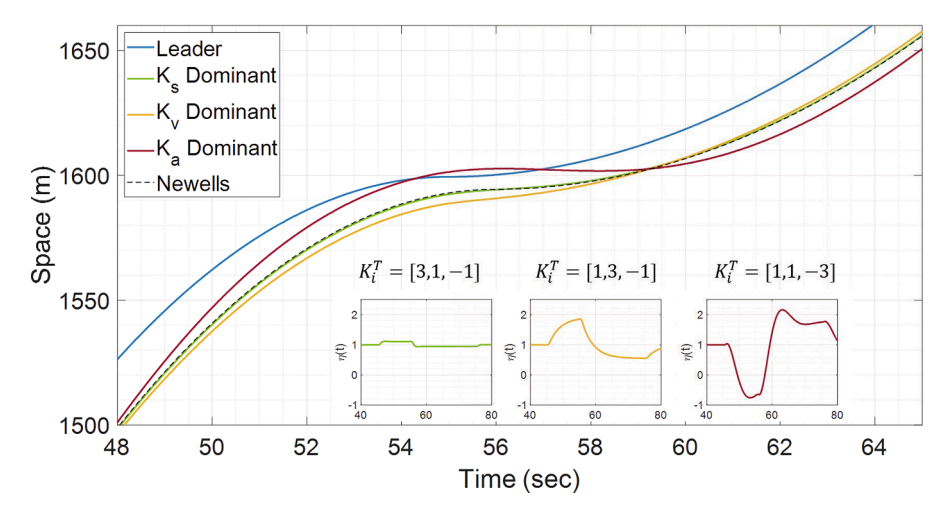


Fig. 6. Effect of each control gain on CF behavior and $\eta(t)$.

Table 2Governing behavior of the control gains in linear controller.

Ki	Coefficient	Controller Command	Effect of $ k_i $ \uparrow
k_s	$\Delta d_i(t)$	Maintain the target spacing	Pushes towards Newell behavior (constant pattern)
$k_{ u}$	$\Delta v_i(t)$	Match the leader's speed	Generates responsive behavior (concave-convex pattern)
k_a	$a_i(t)$	Minimize acceleration	Resists acceleration change (convex-concave pattern)

$$\eta_s(t) = \frac{y_{i-1}(t - \tau^*) - y_i(t)}{\delta^*} \tag{7}$$

3.3. Analysis of Control Mechanism and CF Behavior

To analyze the impact of the controller setting on the CF behavior, we present a twofold investigation: (i) the effect of each control gain on CF behavior and (ii) collective effects of the three control gains. Note that (i) is critical to understanding the physical mechanisms of how the gains govern traffic flow dynamics, more specifically disturbance evolution.

Fig. 6 shows the CF behavior of the linear controller for three setups, each representing a case where one of the three gains is dominant. Though such exaggerated settings may not be implementable in real world, they provide a means to highlight the impacts of each gain in isolation. In Fig. 6 the leader (blue curve) experiences a stop-and-go disturbance with the vehicle cruising at a constant speed of 30m/sec initially, decelerating at $-3m/sec^2$ starting at t=45 for 10 s, accelerating with a magnitude of $1.5m/sec^2$ at from t=55 to t=75 to regain initial speed, and cruising thereafter at constant speed. Note that the sub figures in Fig. 6 show the respective $\eta(t)$ profile for each case. The following observations are notable:

- 1. k_s is the gain responsible for regulating the deviation from target equilibrium spacing $(d_i^*(t))$. It is evident from Fig. 6 that when k_s is dominant, the CF behavior is similar to Newell's (the follower trajectory is derived by shifting the leader trajectory laterally in time by τ^* and vertically in space by δ^*). This is somewhat expected since in Eqn. (2) the target equilibrium spacing based on the constant time-gap policy resembles the formulation of Newell's model. This is consistent with the $\eta(t)$ (green) that is nearly constant around 1.
- 2. k_{ν} is the gain responsible for regulating the speed difference $\Delta v_i(t)$ between the leader (i-1) and follower (i). When the controller is set to be sensitive to the speed difference (i.e., k_{ν} is high), the follower tries to constantly match the leader's speed (follower trajectory is derived by shifting leader trajectory vertically in space by a constant spacing). Looking at the yellow trajectory in Fig. 6, we can see that the follower maintains a larger gap with its leader from early on. As the response to change in speed is immediate, this translates to the η growing (reducing) when the leader reduces (increases) its speed (Note that η is measured at a τ^* time lag). This results in the follower's η showing a concave (leader decelerating) followed by a convex (recovering, leader accelerating) reaction pattern, referred to as the "concave-convex" pattern hereafter.
- 3. k_a regulates the acceleration of the vehicle. To keep the acceleration values low for smoother driving, k_a is always set as a negative value, with the magnitude of the gain representing the sensitivity of the controller to vehicle acceleration. Thus a high $|k_a|$ prompts a stronger reaction by the controller in resisting change in speed. The red trajectory in Fig. 6 illustrates how such behavior manifests. At the start of the oscillation, the follower resists deceleration, resulting in the red trajectory well ahead of the green

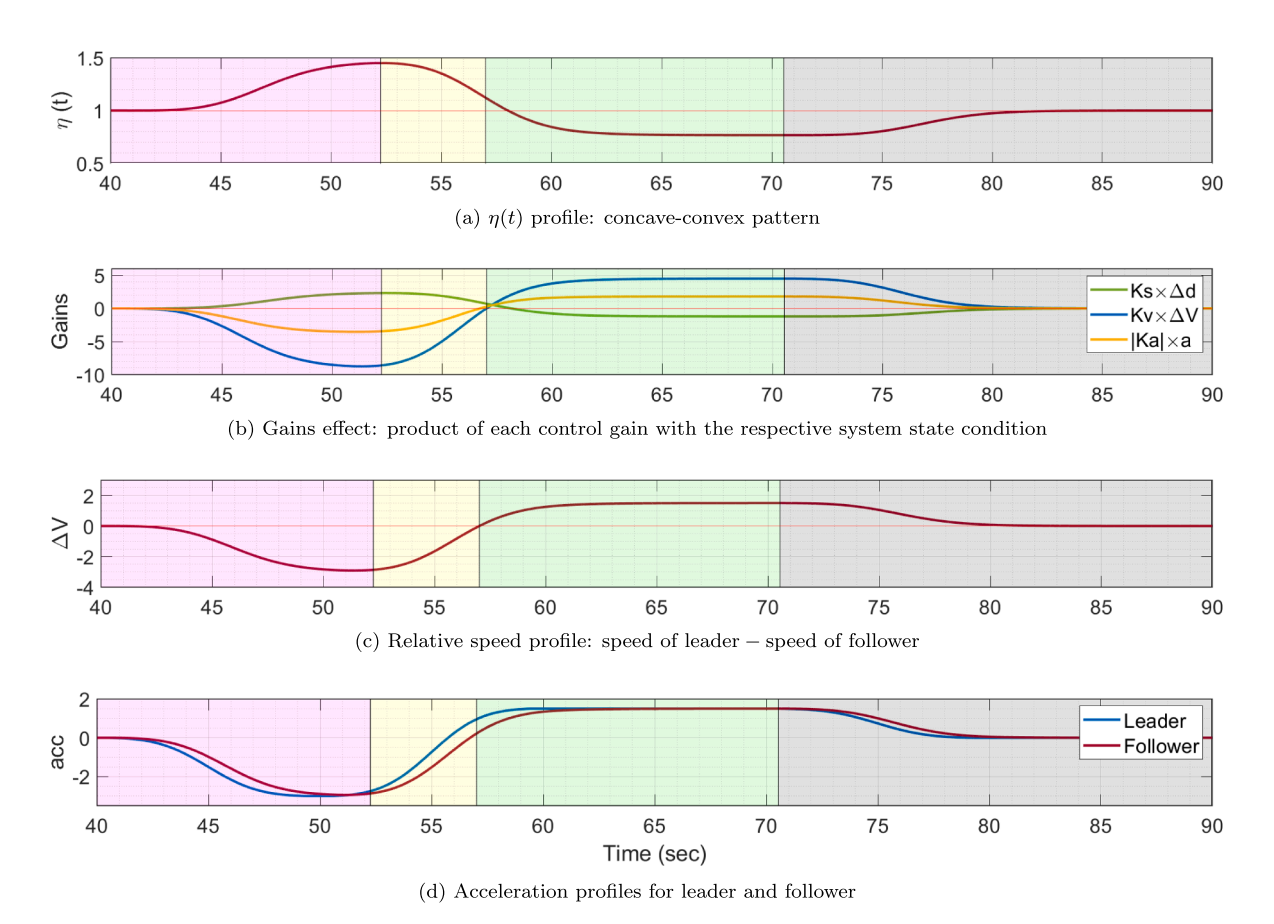


Fig. 7. Collective effects of control gains on $\eta(t)$ for concave-convex pattern; $\mathbf{K}_i^T = [3, 3, -1.2]$.

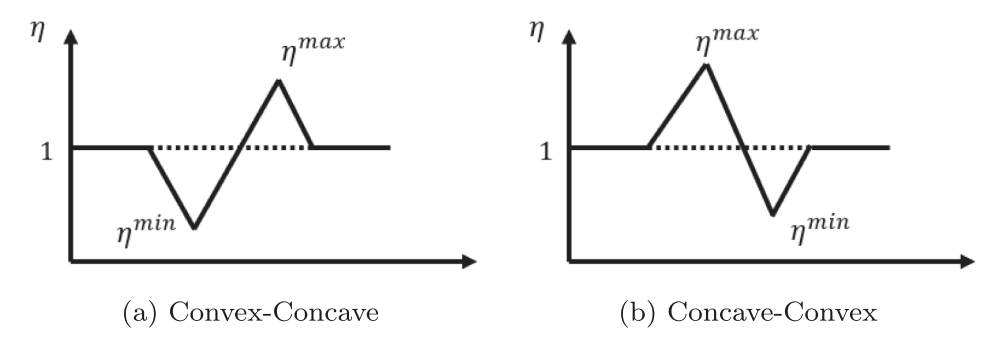


Fig. 8. Reaction patterns, $\eta(t)$, common for linear controllers.

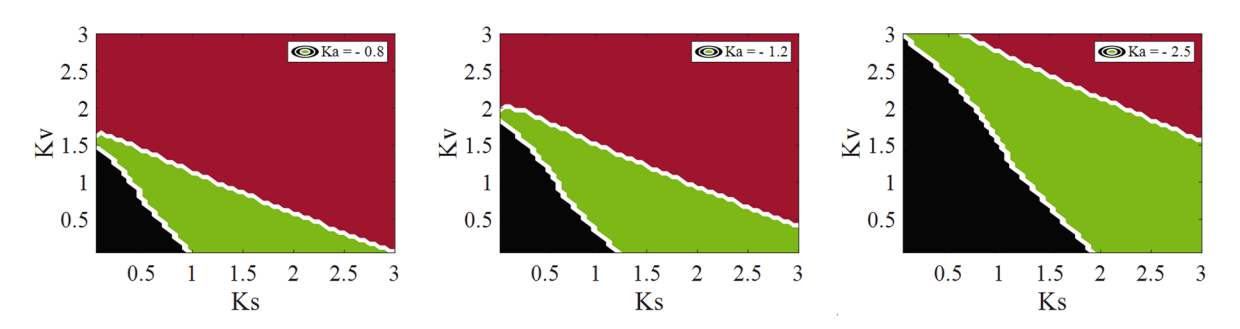


Fig. 9. Mapped relationship between control gains and shape of $\eta(t)$; black (instability region), green (convex-concave), red (concave-convex).

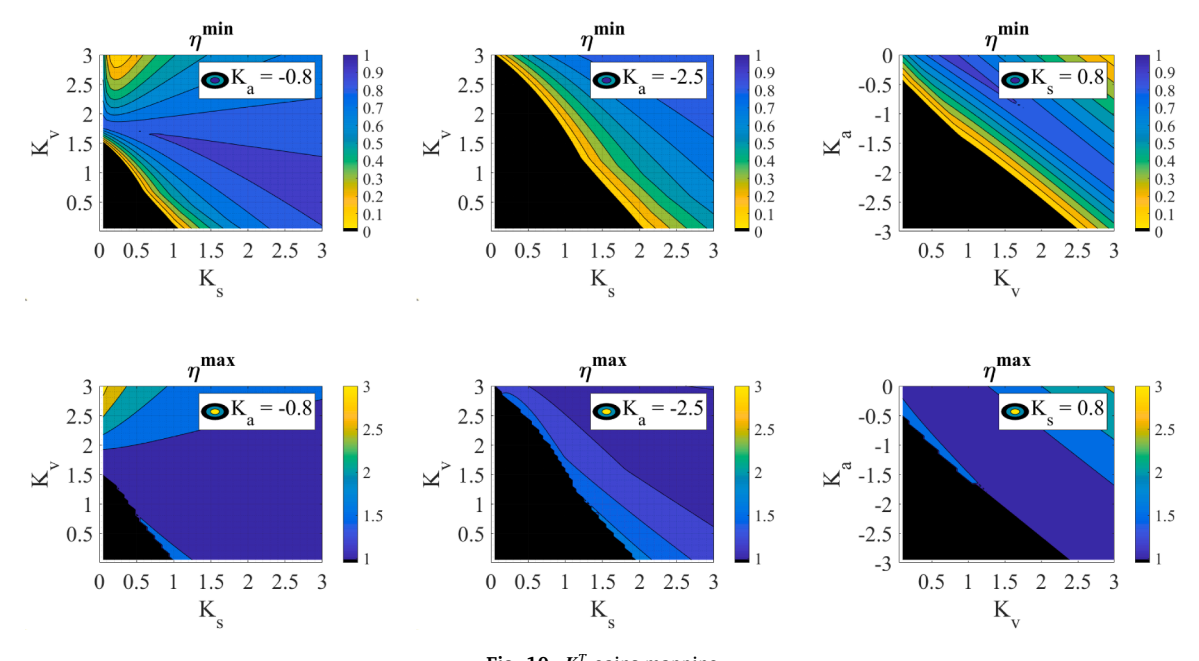


Fig. 10. K_i^T gains mapping.

(dominant k_s) and yellow (dominant k_v) trajectories. In fact, the follower overtakes the leader in this extreme case before the k_a component is eventually overridden by the other components, resulting in a drastic reduction in speed to avoid collision. In the recovery phase, it likewise resists acceleration, resulting in the gap growing substantially before the other gains take precedence and initiate the acceleration phase. This behavior translates to a large convex followed by concave behavior, referred to as the "convex-concave" pattern hereafter.

The effects of individual control gains are summarized in Table 2. Our analysis results suggest that a concave-convex pattern is

desirable for disturbance attenuation. As the yellow trajectory in Fig. 6 shows, a rapid response during deceleration saves the follower from coming to a complete stop (as the leader does), thereby dampening the disturbance to some extent. In contrast, a convex-concave pattern is not desirable in terms of disturbance growth and safety as the red trajectory in Fig. 6 suggests. The follower overtakes the leader (i.e., collision) and comes to a complete stop for a prolonged period.

After analyzing the physical mechanisms governed by each control setting, we now investigate how these settings collectively interact to produce a reaction pattern and govern the CF behavior of the AV. Towards this goal, we analyze the case illustrated in Fig. 7 in details. The figure breaks down four key elements in follower behavior: evolution of $\eta(t)$ (Fig. 7a), contribution of each gain component (gain multiplied by corresponding system state condition (i.e., $k_s \Delta d_i(t), k_v \Delta v_i(t), |k_a|a_i(t)$) (Fig. 7b), speed difference $\Delta v_i(t)$ (Fig. 7c), and the acceleration profile (Fig. 7d).

Fig. 7 presents the temporal evolution of a concave followed by convex reaction pattern (referred to as concave-convex). At the start of the oscillation ($t \approx 42.5$ secs) the controller perceives that ΔV is $\ll 0$ and invokes a deceleration response. Due to the high k_{ν} (blue curve in Fig. 7b), the controller is very responsive and thus the follower decelerates promptly. This k_{ν} dominant mechanism results in a concave pattern evolution, as the follower's rapid response increases the gap from its leader. This can be noted as well in the $k_s \Delta d$ (green curve in Fig. 7b) which is > 0, meaning that the actual separation between the two vehicles ($d_i(t)$) is larger than the desired separation ($d_i^*(t)$). The concavity increases till a maximum value of $\eta^{max} \approx 1.5$, after which a combination of the leader's deceleration starting to taper off and increasing magnitude of the k_s response (since the deviation from ideal spacing is large now), starts influencing the controller behavior, leading to the follower closing back in towards desired spacing. Notably, during this duration (yellow shade), the $\eta(t)$ profile decreases to approach 1 and ΔV approaches 0. At $t \approx 57$ (leader accelerating) the controller perceives that $\Delta V > 0$ and invokes an acceleration response once again reacting promptly due to a strong k_{ν} component. In here, the responsive acceleration maneuver results in convex pattern as the follower increases speed to catch us with its leader.

Note that the detailed physical mechanisms for the convex-concave pattern can be derived using similar logic. For brevity, the details are omitted here.

3.4. Mapping Control Gains to AB CF Parameters

Here we explore the locality of each pattern (seen in Fig. 8) in the large space of control gains, as shown in Fig. 9. The figure shows three primary regions: (1) convex-concave (red region), (2) concave-convex (green), and (3) instability (black). (Weak concavity and weak convexity together represents Newell-like behavior). The black region of instability correspond to scenarios of collisions or even back travel.

A principal insight from this mapped relationship is the switch between concave-convex and convex-concave patterns. It is evident from the figure that increasing k_v (holding other gains constant, i.e., moving vertically upwards in Fig. 9) results in a shift from convex-concave into concave-convex patterns. This is in line with the mechanisms explained in Section 3.3, whereby higher k_v leads to a rapid reaction to the speed change, resulting in an increased gap with its leader during deceleration. Interestingly, this shift occurs at lower k_v with higher k_s , suggesting that the desirable concave-convex pattern can be achieved jointly by higher k_v and k_s . Also evident is that increasing $|k_a|$ (i.e., moving from subplot 1 to subplot 3 while holding k_s and k_v constant) results in a shift from concave-convex into undesirable convex-concave. This, again, is a manifestation of k_a resisting deceleration (acceleration) that leads to follower closing in on (lagging behind) the leader. As expected, high $|k_a|$ coupled with low values of k_s and k_v leads to a large black region.

Next we explore the relationship between control gains setting and the extent of convexity and concavity, i.e., η^{min} and η^{max} . Fig. 10 shows the relationship between η^{min} , η^{max} and the control gains K_i^T . Note that, Figs. (10a, b) show the relationship of K_v , K_s , and η^{min} with different K_a values ($K_a = -0.8$, $K_a = -2.5$). Similarly, Figs. (10d,e) show η^{max} mappings. However, Figs. (10c,f) map the relation between K_a and K_v for a constant K_s value.

As expected, we see that both η^{max} and η^{min} show a monotonic relationship with k_s outside the instability region: an increase in k_s pushes both values towards 1, corresponding to Newell-like behavior. On the other hand, they have non-monotonic relationships with k_v and k_a . While this seems odd at first, it is actually due to the shift in reaction pattern (refer to Fig. 9). Specifically, as k_v increases, η^{min} increases from low values to 1, and then decreases back to low values. The increase in η^{min} occurs in the convex-concave region and marks diminishing convexity during deceleration as $\eta(t)$ approaches the Newell-like behavior. As k_v continues to increase, $\eta(t)$ eventually shifts to concave-convex pattern, and η^{min} now decreases during convex recovery, marking stronger recovery, as the concave-convex pattern becomes stronger. Similar interpretations can be obtained for the η^{max} and the relationships with k_a .

4. Model Predictive Control (MPC) Analysis

In this section, we analyze the CF behavior of MPC-based vehicle control using the AB framework to derive insight into the impact on disturbance evolution. The MPC-based vehicle control can handle multiple objectives and physical constraints. However, the setting for control objectives and constraints can introduce heterogeneity in the CF behavior. Here we focus on four different settings: (i) unbounded acceleration and deceleration rates, (ii) bounded deceleration only, (iii) bounded acceleration only, and (iv) bounded deceleration and acceleration. (i) is considered to examine the basic control mechanisms, particularly in comparison to the linear controller. (ii) is considered since the deceleration behavior during a disturbance is likely to impact string stability. (iii) is considered since it will likely impact the recovery phase of disturbance. For example, Chen et al. (2019) shows that acceleration heterogeneity can lead to traffic void creation and disturbance propagation. (iv) is considered for the compounding effect of both bounds together.

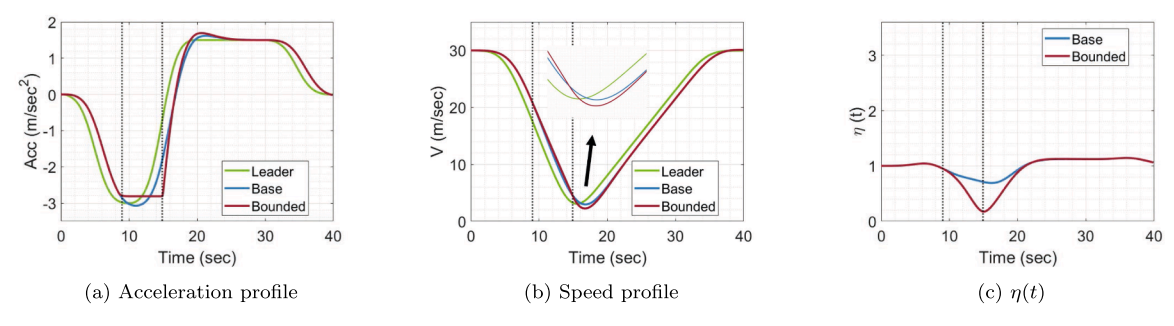


Fig. 11. The effects of bounded deceleration (convex-concave pattern).

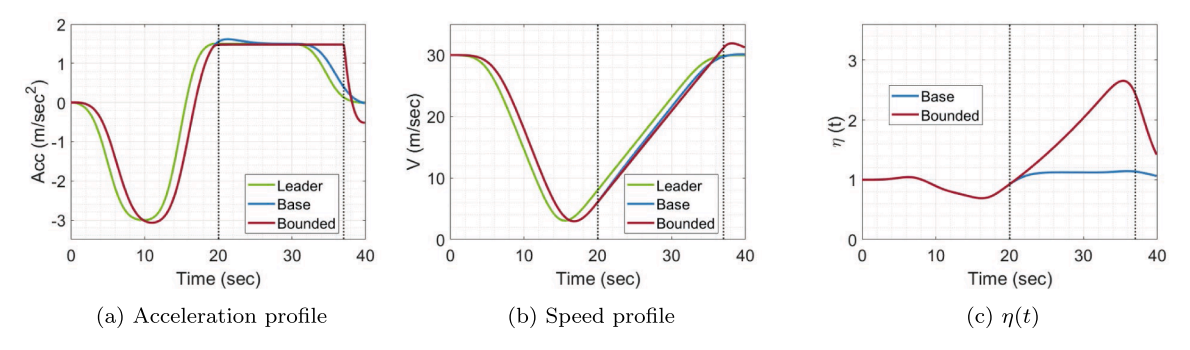


Fig. 12. The effects of bounded acceleration (convex-concave pattern).

4.1. Controller Background

We base our investigation on the state-of-the-art control model designed by Zhou et al. (2019). It formulates an optimal control strategy that considers car-following control efficiency, and driving comfort and fuel efficiency, subject to acceleration/deceleration limits and maximum deviation from target spacing constraints. In short, the MPC formulation builds on the state-space system in Eqn. (4) to develop an optimization framework that seeks to minimize a running cost function at each time step of the prediction horizon given in Eqn. (8), and state constraints given in Eqn. (9). For conciseness we only show the formulations of interest in this paper, and readers are referred to Zhou et al. (2019) for the detailed formulation.

$$\sum_{m=1}^{k_p} L_i(x_{i,k+m}^{p,k}, u_{i,k+m-1}^{p,k}) = (x_{i,k+m}^{p,k})^T Q_i(x_{i,k}^{p,k}) + R_i(u_{i,k+m-1}^{p,k})^2$$
(8)

$$a_{i,min} \leqslant H x_{i,k}^{p,k} \leqslant a_{i,max}$$

$$\Delta d_i^- \leqslant G x_{i,k}^{p,k} \leqslant \Delta d_i^+$$

$$(9)$$

where k is the time step and k_p is the prediction horizon set long enough to circumvent the myopic CF behavior Zhou et al. (2019); Wang et al. (2014); x_i is the system state; u_i is the control input; Q_i and R_i are weight matrices. Note that the system state is defined with the same three components as the linear controller: i.e., $x_i(t) = [\Delta d_i(t), \Delta v_i(t), a_i(t)]$, as this is a common state space used for different

longitudinal control algorithms of AVs.
$$Q_i = \begin{bmatrix} \alpha_{1,i} & \alpha_{2,i} & \alpha_{3,i} \end{bmatrix}$$
; and R_i is a scalar; $a_{i,min}$ and $a_{i,max}$ are the deceleration and acceleration

constraints, respectively; $H = [0, 0, 1]^T$; $(\Delta d_i^-, \Delta d_i^+)$ depict the maximum allowable deviations from target spacing; and $G = [1, 0, 0]^T$. In Eqn. (8) the first term regulates the control efficiency based on the system state, while the second term considers comfort and fuel consumption. In this study, we focus on the former, as it is intrinsically related to the CF behavior. Accordingly, Q_i is of specific interest as it weighs the efficiency of the controller relative to each system state. Specifically, $\alpha_{1,i}$ in Q_i is the weight for deviation from target spacing, $\alpha_{2,i}$ for speed difference, and $\alpha_{3,i}$ for acceleration. To analyze the impact of Q_i setting on the CF behavior, we set the constraints in Eqn. (9) inactive (i.e., unbounded setting) and perform numerical simulations to obtain vehicle trajectories. Then the AB reaction patterns are extracted and analyzed based on the trajectories in similar manners as the linear control analysis in Section 4. We further investigate the bounded setting by limiting the deceleration rate $(a_{i,min})$ or the acceleration rate $(a_{i,max})$. Since an overly-tight constraint on deviation from the target spacing could lead to an infeasible solution, we treat $(\Delta d_i^-, \Delta d_i^+)$ as unbounded and focus on the acceleration and deceleration constraints.

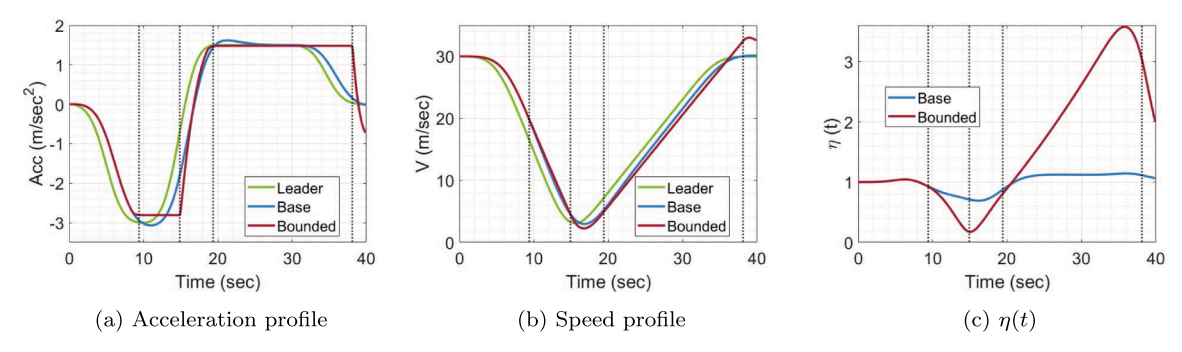


Fig. 13. The compound effects of bounded acceleration and deceleration (convex-concave pattern).

4.2. Effects of Control Weight Matrices and Constraints

With the optimization framework, it is infeasible to analyze the system behavior in a completely analytical fashion. Thus, similar to the approach taken for the linear control, we first perform numerical simulations to extract AV trajectories based on a pre-designed leader trajectory and analyze the trajectories using the AB framework to unveil physical mechanisms to the extent possible. The same leader trajectory as in Section 3 is adopted; $d = -3m/sec^2$, $a = 1.5m/sec^2$, and $am \approx 27m/sec$. Note that due to high computational complexity of MPC, we adopt a smaller-scale simulation than the counterpart in Section 3. The goal here is not to have a complete mapping of the control setting to the AB model, but to investigate the underlying physical mechanisms and gain insights into the differences and similarities between the two control paradigms. Also, to retain a reasonable scope, we assume a system with no communication similar to the setting in Section 3.

4.2.1. Unbounded Setting

Interestingly, the observed behavior under unbounded setting is consistent with that for the linear controller, specifically in Fig. 6 and Table 2. This is expected since the system state x(t) is the same between MPC and linear controller, which effectively gives the state regulator matrices K_i^T (linear controller) and Q_i (MPC) a similar functionality. Thus, one can compare the effects of K_i^T and Q_i on the CF mechanisms analogously: $\alpha_1 := k_s$; $\alpha_2 := k_v$; $\alpha_3 := k_a$. Accordingly, when α_1 is dominant we observe Newell-like behavior, dominant α_2 leads to concave-convex reaction pattern, and dominant α_3 leads to a convex-concave reaction pattern.

While the basic control mechanisms and the resultant $\eta(t)$ appear similar between the two control types, active constraints in the MPC-based controller could significantly influence the CF behavior and alter $\eta(t)$. This is examined next in more detail.

4.2.2. Bounded Setting

Here we examine the individual effects of deceleration and acceleration bounds, and their compound effects in comparison to the base case of unbounded setting. We present the case with a convex-concave reaction pattern, generated by setting $\alpha_1 = \alpha_2 = 1$ and $\alpha_3 = 5$, as an illustrative example. For bounded deceleration, we limit the maximum deceleration at $-2.81 \, m/sec^2$ for the follower while the leader's deceleration can reach $-3 \, m/sec^2$. For bounded acceleration, we bound the maximum acceleration at $1.48 \, m/sec^2$, slightly below the leader's $(1.5 \, m/sec^2)$. Note that we limit the rates slightly above or below to ensure that a feasible solution can be found.

Figs. 11–13 show the resulting acceleration, velocity, and $\eta(t)$ profiles for the bounded deceleration (Fig. 11), bounded acceleration (Fig. 12), and compound effects with both bounds active (Fig. 13). For the effects of bounded deceleration, at $t\approx 9$ sec, the follower reaches the deceleration bound while the leader continues to decelerate further; see Fig. 11a. This evidently leads the gap to close sharply, causing a sharper decrease in $\eta(t)$ compared to the base case (blue curve); see Fig. 11c. Moreover, to compensate for the limited deceleration, the follower stays at the bounded rate for an extended period, lasting from $t\approx 9$ till $t\approx 15$, which results in significant convexity in $\eta(t)$. This causes further speed reduction (the minimum velocity of the follower (2.25 m/sec) drops below that of the leader (3 m/sec) and that of the base case (2.96 m/sec)), and the control becomes unstable; see the zoomed-in figure insert in Fig. 11b for the velocity. Interestingly, the transition from deceleration to acceleration happens faster (i.e., larger magnitude of jerk) than the base case, and the vehicle enters the acceleration phase slightly sooner. Both the base case and bounded deceleration case have an over-shoot in acceleration, more so for the bounded deceleration case. The effect of bounded deceleration lasts until $t\approx 23$.

With the bounded acceleration (Fig. 12), we see the effect in the recovery phase. With the bound, the acceleration rate does not exhibit overshooting but stays at the bounded rate for an extended period (from $t \approx 20$ till $t \approx 37$); see Fig. 12a. The lower acceleration evidently increases the gap with the leader, as the follower is not able to match the increase in speed of the leader. A larger gap gives rise to more drawn out acceleration at its maximum value and eventually to greater speed than the leader (and the base case) toward the end ($t \approx 37$) to close the extra gap, causing an overshoot of speed and prolonged recovery; see Fig. 12b. The increasing gap, coupled with the prolonged recovery, induces substantial concavity in $\eta(t)$ in the recovery phase, as shown in Fig. 12c.

In the examples above, the periods of the bounded deceleration and acceleration effects slightly overlap (the former ending at $t \approx 22$ sec, and the latter beginning at $t \approx 20$ sec). This indicates that a compound effect is possible: the bounded deceleration can affect the recovery phase and thus, when and how long the acceleration bound will take effect. This compound effect is evident in Fig. 13. The

acceleration bound becomes active earlier and lasts longer than the bounded acceleration only case (from $t \approx 19$ to $t \approx 38$); see Fig. 13a. With the combination of lower minimum speed and bounded acceleration, the vehicle lags further behind in speed recovery, eventually ending up with an even greater overshoot than the previous case; see Fig. 13b. All these lead to much greater concavity and longer recovery, as evident in Fig. 13c.

A similar analysis was conducted for the concave-convex pattern. The results remain consistent in the sense that bounded deceleration induces convexity during the deceleration phase, whereas bounded acceleration induces concavity in the recovery phase. Interestingly, the bounded deceleration shaves off a significant portion of concavity but does not eliminate the concavity in its entirety in some cases. Likewise, the bounded acceleration turns a large, but not the entire, portion of convexity into concavity, leaving the reaction pattern more complex. Note that the extent of these effects and the compound effect depends on the bounds setting and disturbance characteristics.

5. Prediction Models for Car-following Behavior

Section 3 and Section 4 established a clear mapping between the control parameter setting and $\eta(t)$. We have shown how a parameter setting results in a unique $\eta(t)$ evolution, characterized by its shape and parameter values (η^{min}, η^{max}). The natural next step toward scaling up to the traffic-level impacts is to quantify this relationship through a prediction model. The basic idea is that given the control parameter setting (e.g., K_i^T, Q_i) and the leader's behavior (d, a, am), we should be able to predict the $\eta(t)$ shape, as well as η^{min} and η^{max} . This is achieved through a bi-level modeling framework: (i) classification model for $\eta(t)$ reaction pattern (convex-concave vs. concave-convex), and (ii) multivariate convoluted prediction model for η^{min} and η^{max} . Coupled together, we can predict the $\eta(t)$ profile.

Note that given the availability of both empirical and extensive simulation data, our presentation of the formulation and model validation is oriented toward the linear controller. Nonetheless, the modeling framework is general and can be applied to other controllers (e.g., MPC-based control) by changing the input variables and/or adjusting the construction of information sharing (i.e., convolution construction).

5.1. Logistic Classifier

The first step of the prediction is to determine the reaction pattern of $\eta(t)$. From Fig. 9, we can see (i) two unique shapes in general, concave-convex and convex-concave, and (ii) linearly separable regions. Thus, this problem boils down to a binary classification problem. Accordingly, the linear separation between the shapes entails the use of a linear classifier, specifically the logistic classifier. For brevity, the formulation for the logistic classifier is omitted, as it is a widely known model Phillips et al. (2015); Allwein et al. (2000), and our approach is consistent with the basics of the model. In essence, the logistic classifier takes an input vector $\mathbf{x} = [k_s, k_v, k_g, d, a, am]$ and classifies the $\eta(t)$ profile as either convex-concave or concave-convex.

5.2. Multivariate Gaussian Process (MGP) Formulation

The predictive model envisioned in this study must be able to characterize the inherent correlation between the two outputs, η^{min} and η^{max} , that occur in the dynamic process. This is achieved through the multivariate (also known as vector-valued or multitask) Gaussian process (MGP) (Alvarez and Lawrence, 2009; Zhao and Sun, 2016). Alternative approaches to multi-output regression based on deep neural networks have been proposed in recent years, but they suffer from drawbacks in uncertainty propagation across outputs (e.g., due to lack of uncertainty quantification), which occurs naturally in MGP due to their Bayesian interpretation (Rasmussen, 2003). Rethinking Neural networks from a Bayesian perspective (Kendall and Gal, 2017) have shown promise, but their extensions to a multitask setting has still not been tackled. In light of this, we adopt the MGP model.

The \mathscr{MSP} model for the linear controller includes six inputs: $x = [k_s, k_v, k_a, d, a, am]$, and two outputs: $y_1(x) := \eta^{min}(x)$ and $y_2(x) := \eta^{max}(x)$. Correspondingly, for each output our data is denoted as $\mathscr{D} = \{D_1, D_2\}$ such that $D_i = \{(y_i, X_i)\}$ where $y_i = [y_1^1, y_1^2, ..., y_i^{p_i}]^t$, $y_i^c := y_i(x_{ic}), X_i = [x_{i1}, ..., x_{ip_i}]^t$ and p_i represents the number of observations for output $i \in \{1, 2\}$. We also let $y = [y_1^t, y_2^t]$ and $X = [X_1^t, X_2^t]^t$ to concatenate all the output and input data respectively.

Given the two output functions, $y_1(x)$ and $y_2(x)$ and input x, the MGP is defined as

$$\begin{bmatrix} y_1(\mathbf{x}) \\ y_2(\mathbf{x}) \end{bmatrix} = \begin{bmatrix} f_1(\mathbf{x}) \\ f_2(\mathbf{x}) \end{bmatrix} + \begin{bmatrix} \epsilon_1(\mathbf{x}) \\ \epsilon_2(\mathbf{x}) \end{bmatrix} = \mathscr{F}(\mathbf{x}) + \mathscr{E}(\mathbf{x})$$
(10)

where $\mathscr{F}:\mathscr{R}^D\to\mathscr{R}^2$ is a multivariate process with covariance $\operatorname{cov}_{ij}^f(x,x')=\operatorname{cov}_{ij}^f\left(f_i(x),f_j(x')\right)$ and zero mean for all $x,x'\in\mathscr{X},i,j\in\{1,2\}$ and $\in_i(x)\sim\mathscr{N}(0,\sigma_i^2)$ denotes additive noise. Note that Eqn. (10) is a general decomposition of an \mathscr{MSP} and will recede to a \mathscr{SP} with one output. We also note that the zero-mean assumption is most commonly used since the \mathscr{SP} is a non-linear and non-parametric functional representation, where the mean has a minor effect on predictions (i.e. posterior). Please refer to Rasmussen (2003) for more details.

The MSP assumes that the predicted value for any new observed output $\{y_i(x_0): i \in \{1,2\}\}$ with a input vector $x_0 \in \mathcal{X}$, and the previous observations y, have a joint distribution given as:

Table 3 Prediction errors on simulated data of $\eta(t)$ shape, η^{min} , and η^{max} .

Test	% Wrong Classifications	MAE	
	Logistic Classifier	η^{min}	η^{max}
Cross Validation	3.4	$0.002(\pm0.0008)$	$0.007(\pm0.003)$
Test Trajectory 1	5.9	$0.004(\pm0.002)$	0.01(±0.008)
Test Trajectory 2	15.7	$0.13(\pm 0.08)$	$0.29(\pm0.18)$

$$\begin{pmatrix} \mathbf{y} \\ y_i(\mathbf{x}_0) \mid D \end{pmatrix} \sim \mathcal{N} \begin{pmatrix} \mathbf{0}_{p+1}, & \begin{bmatrix} \mathbf{C}_{ff} + \mathbf{\Sigma} & \mathbf{C}_{ff_i^0} \\ \mathbf{C}_{ff_i^0}^t & \mathbf{C}_{f_i^0 f_i^0}^t + \sigma_i^2 \end{bmatrix} \end{pmatrix}$$

$$(11)$$

where $p = p_1 + p_2$ and $f = [f_1^t, f_2^t]^t$ are the latent variables corresponding to the observed noisy output y, such that $f_i^c := f_i(x_{ic})$ and $f_i = f_i(X_i)$. The $C_{ff} \in \mathscr{R}^{p \times p}$ is the covariance matrix relating all input points for all outputs with $\cot^f_{ij}(x,x')$; $\Sigma = diag[\sigma_1^2 I_{p_1}, \sigma_N^2 I_{p_2}]$ is a block diagonal matrix, in which the ith block corresponds to a $p_i \times p_i$ matrix; $C_{ff_i^0} = [C_{f_1,f_i^0}^t, ..., C_{f_N,f_i^0}^t]^t$ where $f_i^0 := f_i(x_0)$; $C_{f_c,f_i^0} = [\cot^f_{f_i(x_0,x_{c1})}, ..., \cot^f_{f_N,f_i^0}]^t$; and $C_{f_i^0,f_i^0} = \cot^f_{ii}(x_0,x_0)$. Following the conditional probability theory, the predicted distribution of $y_i(x_0)$ denoted as $pr(\cdot|y)$ is given as:

$$pr(y_i(\mathbf{x}_0)|\mathbf{y}) = \mathcal{N}\left(C_{ff_i^0}^t(C_{ff} + \mathbf{\Sigma})^{-1}\mathbf{y}, C_{f_i^0f_i^0} + \sigma_i^2 - C_{ff_i^0}^t(C_{ff} + \mathbf{\Sigma})^{-1}C_{ff_i^0}\right)$$
(12)

Note that the mean does not require normality assumptions, as it can be derived from the best empirical linear unbiased predictor (EBLUP) Stein and Corsten (1991).

As shown in Eqn. (12), the sharing information is achieved through $\cot_{ij}^f(x,x')$. The success of \mathscr{MSP} s is mainly attributed to the convolution process (\mathscr{CP}) construction of this covariance, which enables the outputs to possess both shared and unique features Alvarez and Lawrence (2011). The basic idea of the \mathscr{CP} is that a \mathscr{CP} , $f_i(x)$, can be constructed by convolving a smoothing kernel $k_i(x)$ with a latent \mathscr{CP} process X(x). This is equivalent to stimulating a stable linear filter where $k_i(x)$ is the impulse response (stability only requires $\int_{-\infty}^{\infty} |k_i(u)| du < \infty$). Based on the \mathscr{CP} , one can construct an \mathscr{MSP} through a sharing multiple latent function across all outputs, $f_i(x)$. As a result, all outputs can be expressed as jointly distributed \mathscr{CP} , i.e., an \mathscr{MSP} .

$$f_i(\mathbf{x}) = \sum_{q=1}^{Q} K_{qi}(\mathbf{x}) \otimes X_q(\mathbf{x}) = \sum_{q=1}^{Q} \int_{-\infty}^{+\infty} K_{qi}(\mathbf{x} - \mathbf{u}) X_q(\mathbf{u}) d\mathbf{u}$$
(13)

where \otimes denotes a convolution. A key feature in Eqn. (13) is that information is shared through different kernels $K_{qi}(x)$, hence offering increased flexibility in accounting for heterogeneity and allowing the data to speak for itself (i.e., not forcing correlation). Given Eqn. (13) and assuming that X(x) are independent white noise processes with $cov(X_i(x), X_i(x')) = \delta(x - x')$ and δ is the Dirac delta function, we have

$$\operatorname{cov}_{ij}^{f}(\boldsymbol{x}, \boldsymbol{x}') = \sum_{q=1}^{Q} \int_{-\infty}^{\infty} K_{i}(\boldsymbol{u}) K_{j}(\boldsymbol{u} - \boldsymbol{d}) d\boldsymbol{u}$$
(14)

where $d = x^{'} - x$ is the displacement vector.

Finally, a smoothing kernel structure need to be specified for the model. The most commonly used kernel is the Gaussian kernel in Eqn. (15), which is capable of representing any family of continuous and differential function as it is equivalent to an infinite summation of basis function in a Bayesian linear regression setting Rasmussen (2003).

$$K_{qi}(x) = \alpha_{qi} (4\pi)^{\frac{D}{4}} |\Lambda_{qi}|^{-\frac{1}{4}} \mathcal{N}(\mathbf{x}|\boldsymbol{\theta}, \Lambda_{qi}^{-1})$$

$$\tag{15}$$

where Λ_{ai} is a diagonal matrix with a length scale parameter at each dimension. Then by plugging in Eqn. (15) into Eqn. (14), we have

$$\operatorname{cov}_{ij}^{f}(\boldsymbol{x}, \boldsymbol{x}') = \sum_{q=1}^{Q} \frac{2^{\frac{D}{2}} \alpha_{qi} \alpha_{qj} |\Lambda_{qi}|^{\frac{1}{4}} |\Lambda_{qj}|^{\frac{1}{4}}}{|\Lambda_{qi} + \Lambda_{qi}|^{\frac{1}{2}}} \exp\left(-\frac{1}{2} \boldsymbol{d}' \Phi_{ij}^{-1} \boldsymbol{d}\right)$$

$$\tag{16}$$

where $\Phi_{ij}^{-1} = \left(\Lambda_{qi}^{-1} + \Lambda_{qj}^{-1}\right)^{-1} = \Lambda_{qi} \left(\Lambda_{qi} + \Lambda_{qj}\right)^{-1} \Lambda_{qj}$. We note that the marginal covariance $\operatorname{cov}_{ii}^f(x, x') = \sum_{q=1}^Q \alpha_{qi}^2 \exp(-\frac{1}{4} d^t \Lambda_{qi} d)$ is the commonly used covariance Gaussian form in the univariate process.

The MSP is then parametrized through the kernel parameters θ_f and the noise measurement $\sigma = \{\sigma_1, ..., \sigma_N\}$. Accordingly, we

Table 4Empirical characteristics of lead vehicle under disturbance.

Feature	Mean	STD
Deceleration rate (d) (m/s^2)	0.80	± 0.32
Acceleration rate (a) (m/s^2)	0.59	± 0.20
Oscillation amplitude (am) (m/s)	3.17	± 1.16

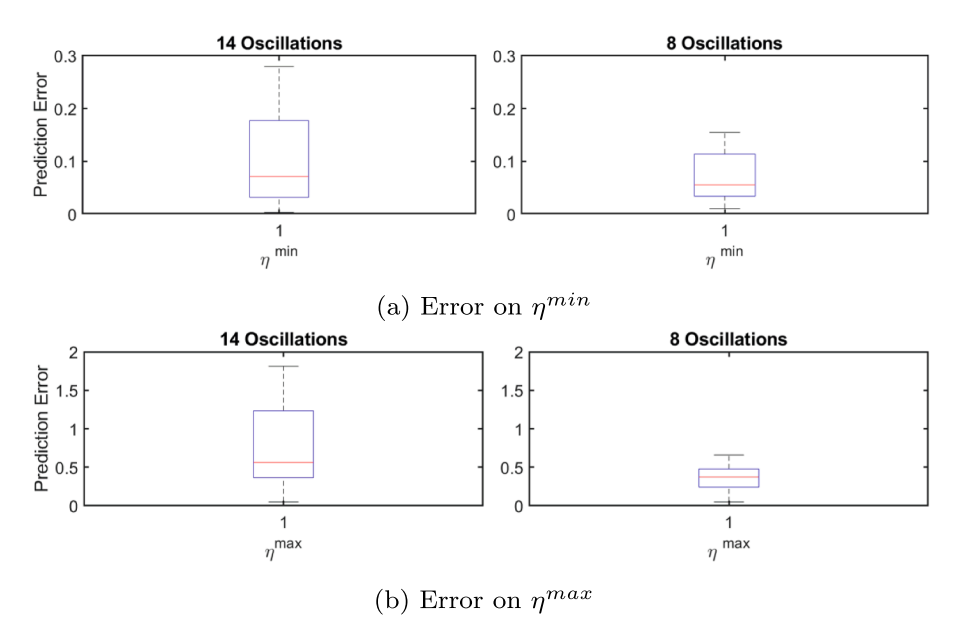


Fig. 14. Prediction errors on empirical data of η^{max} and η^{min} .

denote the parameters $\theta = \{\theta_t^t, \sigma^t\}^t$. Now, with our observed data $\mathcal{D} = \{\mathcal{D}_t, \dots, \mathcal{D}_N\}$, the \mathcal{MGP} likelihood function is given as

$$\mathcal{L}(\theta; \mathcal{D}) = (2\pi)^{-P/2} |C_{ff} + \Sigma|^{-1/2} \times exp(-y(C_{ff} + \Sigma)^{-1}y^t/2)$$

$$\tag{17}$$

The parameters are thus estimated by minimizing the negative log-likelihood function $\ell(\theta; \mathscr{D}) = -\log \mathscr{L}(\theta; \mathscr{D})$. Then, up to a constant $\ell(\theta; \mathscr{D}) = \frac{1}{2} \langle Y, (C_{ff} + \Sigma)^{-1} \rangle + \frac{1}{2} \log |C_{ff} + \Sigma|$, where we define the operator $\langle W, W' \rangle = trace(WW')$ and $Y = yy^t$. Notably, such minimization in a very high dimensional space faces some challenges. Below are some remarks in that regard:

Some remarks on the developed model:

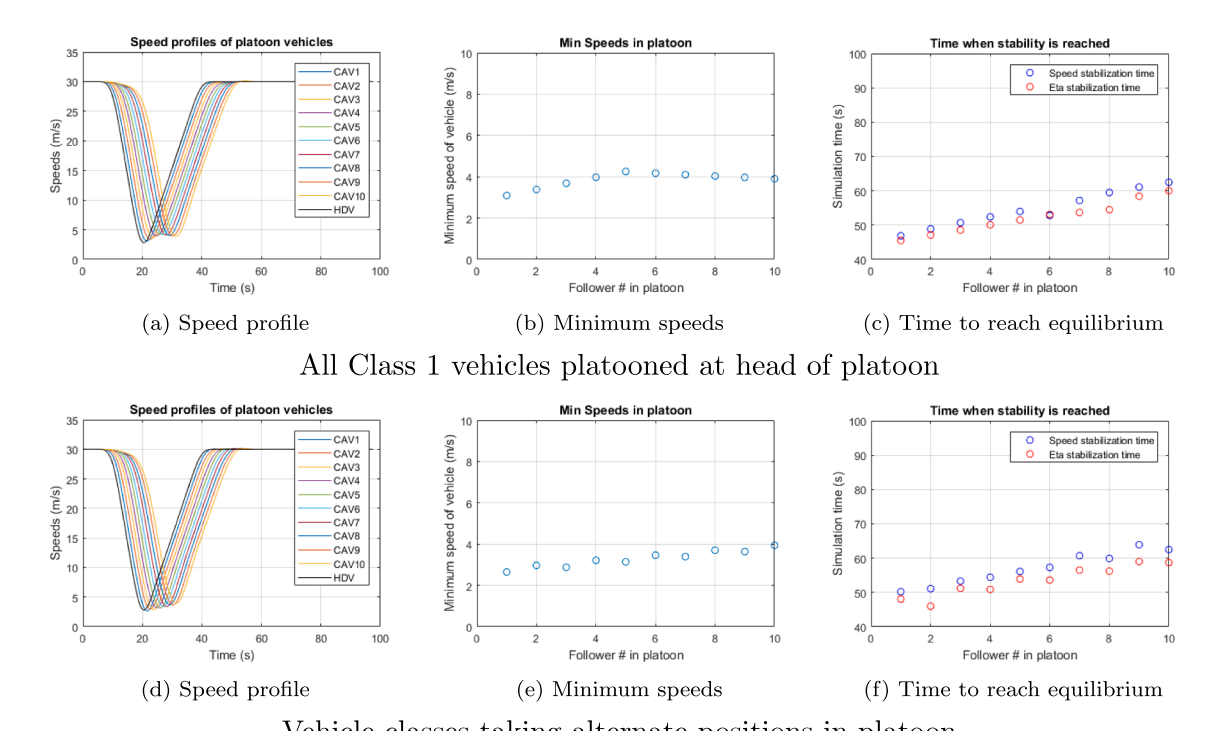
- 1. On computational complexity: Much like a univariate \mathcal{GP} , the \mathcal{MGP} has a cubic complexity of $O(p^3)$. This is mainly due to the inversion of $C_{ff} + \Sigma$. In cases of large data sets (i.e., large p), one can resort to the rich literature on sparse approximate inference in \mathcal{GP} Alvarez and Lawrence (2009); Damianou et al. (2016); Zhao and Sun (2016); Snelson and Ghahramani (2006). The literature is mainly based on estimating the covariance matrix $C_{ff} \approx K_{pz}K_{zz}^{-1}K_{zp}$ as a low rank alternative. Here z denotes a set of inducing points with cardinality(z) = $p_z \ll p$. We refer readers to the survey Liu et al. (2020) in case such approximation is needed. This could be particularly useful in case of very large data set used to train the model.
- 2. On number of latent functions: This remains an open question in literature. Yet, most papers in this field choose Q = 1 and let the kernels handle heterogeneity in the data. Recently, theoretical results by Burt et al. (2019) hinted to the fact that using Q = 1 might be sufficient in most cases, even in inducing point approximations where $p_z = O(\log p)$ would suffice.

5.3. Validation using Simulated Data

The prediction method, coupling the logistic classifier and MSP, is validated by simulated data as well as empirical data. This section presents the validation results using simulated data. Two validation approaches are taken: (i) classic cross-validation on the simulated data and (ii) testing via new trajectories simulated with new lead vehicle settings. To train our model, we sample randomly 200 different combinations of control gains (K_i^T) for the linear controller for each pre-designed leader trajectory (35 trajectories in total). Note that due to the $O(p^3)$ complexity of the MSP, the training time is significant. However, the use of stochastic gradient

Table 5Details on experimental setup.

Scenario	Description	Class 1	Class 1 Vehicle			Class 2 Vehicle		
		k_s	$k_{ u}$	k_a	k_s	$k_{ u}$	k_a	
1	Both controllers well within concave-convex region	1.5	2.5	-0.8	1.5	1.5	-0.8	
2	One in each region: average behavior dominated by concave-convex	1.5	1.5	-0.8	1.5	0.75	-0.8	
3	One in each region: average behavior dominated by convex-concave	1.5	1.0	-0.8	1.5	0.25	-0.8	
4	Both within convex-concave region	1.5	0.75	-0.8	1.5	0.25	-0.8	



Vehicle classes taking alternate positions in platoon

Fig. 15. Impact of ordering of vehicles in platoon - Scenario 2.

descent (SGD) speeds up the training process. In total, the chosen data set is a (7000×8) matrix. We then randomly split the data into training (75%) and testing sets (25%) (this is done to perform the twofold cross validation).

For the second method of validation, we designed two new lead vehicle trajectories and simulated 1000 new observations. The first test trajectory is characterized by $d=-1.8m/sec^2$, $a=1m/sec^2$ and am=15m/sec. The second test trajectory is characterized by $d=-7m/sec^2$, $a=6m/sec^2$ and am=27m/sec. Note that the second test trajectory is purposely designed for an extreme scenario, with the acceleration/deceleration rates beyond the typical values in the training set, to test the model's ability to extrapolate. The trained prediction models are then tested on the new trajectories. Table 3 summarizes the findings and report the percentage of wrong classifications for the logistic classifier and the Mean Absolute Error (MAE) for the MSP. The validation results demonstrate the power of the models in predicting the reaction pattern, and η^{max} and η^{min} . Particularly, it is evident that the MSP learns effectively the functional correlation between η^{max} and η^{min} . Notably, the errors for the second test trajectory are higher, as expected under extreme extrapolation; nonetheless, the performance is still reasonable.

5.4. Validation using Empirical Data

We further validate the prediction method using the empirical data with different oscillations scenarios in the MA experiments. This is done through two steps: (i) approximate the control gain parameters of the ACC vehicle from the MA experiments assuming that it is operating under a linear controller and (ii) predict the $\eta(t)$ shape and parameters. A total of 14 oscillation scenarios are fed into the linear controller (in Eq. (4)))) to calibrate the control gain parameters for the ACC vehicle. The characteristics of these oscillations are

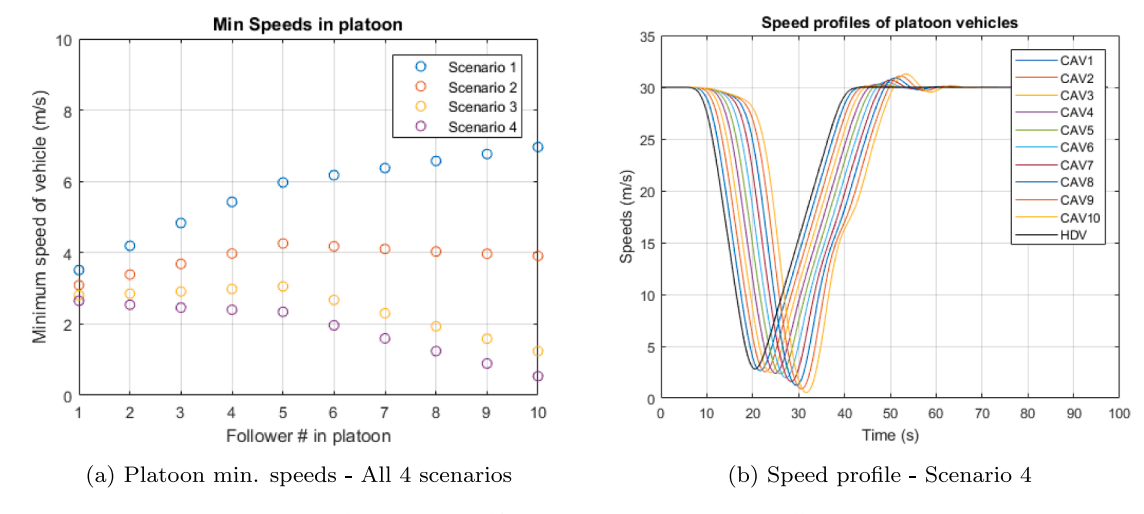


Fig. 16. Impact of heterogeneous composition on traffic.

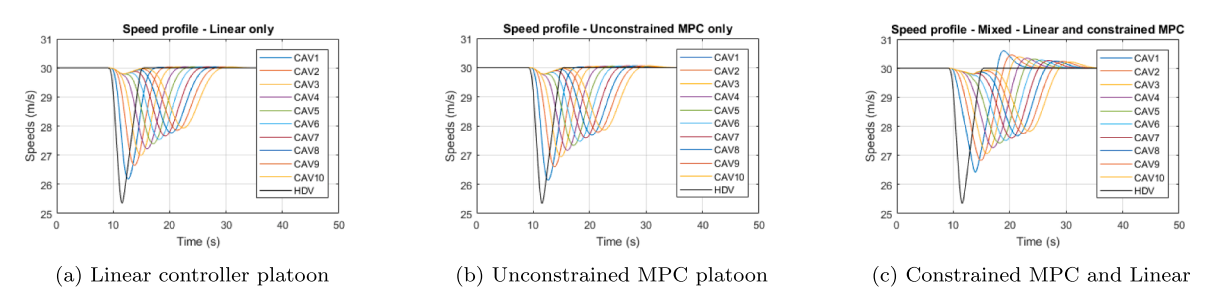


Fig. 17. Speed profiles - Impact of constrained MPC.

summarized in Table 4. The calibration follows the general procedure of the frequency domain method in Ozdemir and Gumussoy (2017). The key idea is to firstly characterize the frequency domain CF behavior using the empirical frequency response function of the ratio between the accelerations of a follower and its leader. The empirical frequency response function is thus represented by amplification ratios and phase shifts under a range of frequencies of interest. Here we focus on 0 to 3 Hz, which is the normal scale of the acceleration in the empirical data. Then the calibration process essentially aims to find a set of control parameters that can best reproduce the empirical frequency response. Readers are referred to Ozdemir and Gumussoy (2017) for more details. The calibrated control gains (k_s, k_v, k_a) are (0.14, 0.62, -0.2), respectively. The calibration error is measured by the H_2 norm of the difference between the empirical and calibrated frequency response. The MAE of the calibration error is 0.11 (min 0.01, max 0.34) in the investigated frequency range. Note that the calibration error for empirical frequency response function typically ranges from 0 to 1. Therefore, the calibration result is reasonable, indicating that the CF behavior of the commercial ACC can be reasonably described by the linear controller assumed in this study.

For validation, we employ the trained models to predict the $\eta(t)$ reaction pattern, η^{min} , and η^{max} using the calibrated control gains and the lead-vehicle characteristics of the ACC vehicle as inputs. Notably, all 14 oscillations exhibit convex-concave reaction patterns, and the logistic classifier was able to classify the pattern for all the cases. For the MSP model, we observe the average errors of 0.09 for η^{min} and 0.75 for η^{max} . The performance for η^{min} , which occurs in the deceleration phase, is particularly promising. Predictions on η^{max} , however, have a lower performance. Upon inspection of the 14 oscillations, we noticed that 6 of them were characterized by high acceleration rates ($\approx 0.8m/s^2$) in the recovery phase. In the response of the ACC, however, the maximum acceleration appears to be bounded around $0.5m/s^2$, which resulted in large η^{max} values and delayed recovery. This type of behavior was not captured in model training. Fig. 14 presents box plots for errors for all 14 oscillations vs. 8 oscillations excluding these special cases. As expected, while the performance of η^{min} remains relatively the same (average error = 0.07; see Fig. 14a), the performance of η^{max} improves significantly (average error = 0.36; see Fig. 14b). The findings suggest that the developed prediction models show great promise in real-life applications but should be further enhanced through training with larger, more comprehensive data sets.

6. Traffic Level Implifications

In this section we explore how the CF behavior translates to traffic wide impacts. While the string stability and local stability of some controller types (available for linear controllers, scarce for MPC-based controllers) in homogeneous traffic is well studied, we

wish to investigate the impact from traffic flow perspective, considering how AVs with different control settings may interact.

6.1. Linear Controller

To gain traffic wide impacts, we set up numerical simulation experiments where a 10-vehicle platoon of AVs is following a leader with a predetermined trajectory (consistent with the one used in earlier sections: $d = -3m/sec^2$, $a = 1.5m/sec^2$, am = 27m/sec). The vehicles in the platoon belong to one of two classes (with different control parameter settings). For illustration, we select four representative class pairings to capture multiple interactions as shown in Table 5, with each representing different regions of behavior shown in Fig. 9. Essentially, we fix $k_s = 1.5$, $k_a = -0.8$ and vary k_v in the range of (0.25, 2.5). The results based on other pairings are qualitatively consistent. Note that based on the string stability condition defined in Zhou and Ahn (2019), gains that result in string stable solutions are contained within the concave-convex (red) region. A general trend observed is that traffic disturbance dampens (amplifies) with concave-convex (convex-concave) reaction patterns; i.e., minimum speeds and time to return to equilibrium increase (decrease) as we move upstream. This is in line with local and string stability conditions for linear controller in Zhou and Ahn (2019). The four studied scenarios are described below:

The first experiment studies the vehicle ordering impact within the heterogeneous platoon. Specifically, we consider two platoon compositions: (i) AVs from a single type congregate together, and (ii) AVs from different classes (control settings) intermingle. For the first composition, we consider two different cases: 5 vehicles of Class 1 followed by 5 vehicles from Class 2 (or visa versa). In the second composition, Class 1 and Class 2 vehicles alternate.

Fig. 15 shows the resulting speed profiles, evolution of minimum speeds within the platoon, and time to reach equilibrium within the platoon. The main insight is that vehicle ordering affects how the disturbance magnitude (speed reduction) evolves from vehicle to vehicle. However, the average behavior (based on the minimum speed and time to reach equilibrium for the final vehicle in the platoon) is independent of the ordering. This is not unexpected from a linear controller. It is important to note, however, that the linear controller is often accompanied with other complementary lower level controllers in a real implementation on a road vehicle (such as acceleration and speed constraints). Exploring such interactions remains outside the scope of this study.

In the second experiment, we look at the impact of the platoon composition (by changing the parameter setting according to Table 5) on disturbance evolution. Here, the ordering is five class 1 vehicles followed by five class 2 vehicles (as defined in each scenario). The evolution of minimum speed over the platoon for each scenario is presented in Fig. 16a. As stated earlier, control settings that fall within the concave-convex (convex-concave) reaction region are expected to result in disturbance dampening (amplification). This is seen in the results with the disturbance getting dampened in the Scenarios 1 and 2 that involve dominant concave-convex behaviors. Further, the dampening is much more efficient in Scenario 1 due to the stronger concave-convex reaction. Conversely, the disturbance is seen to amplify in Scenarios 3 and 4 where convex-concave is the dominant behavior. In addition, where convex-concave vehicles amplify the disturbance, varying extents of speed overshooting (speed increasing over the initial speed and effectively extending the disturbance by adding a second smaller disturbance) is seen (see Fig. 16b).

These experiments support the insights that were derived in earlier sections, as well as present a framework for a more detailed analysis of traffic flow impacts of heterogeneous AVs. Insights gathered here, can guide the design of desired controller behavior with traffic-level performance in mind (described through $\eta(t)$).

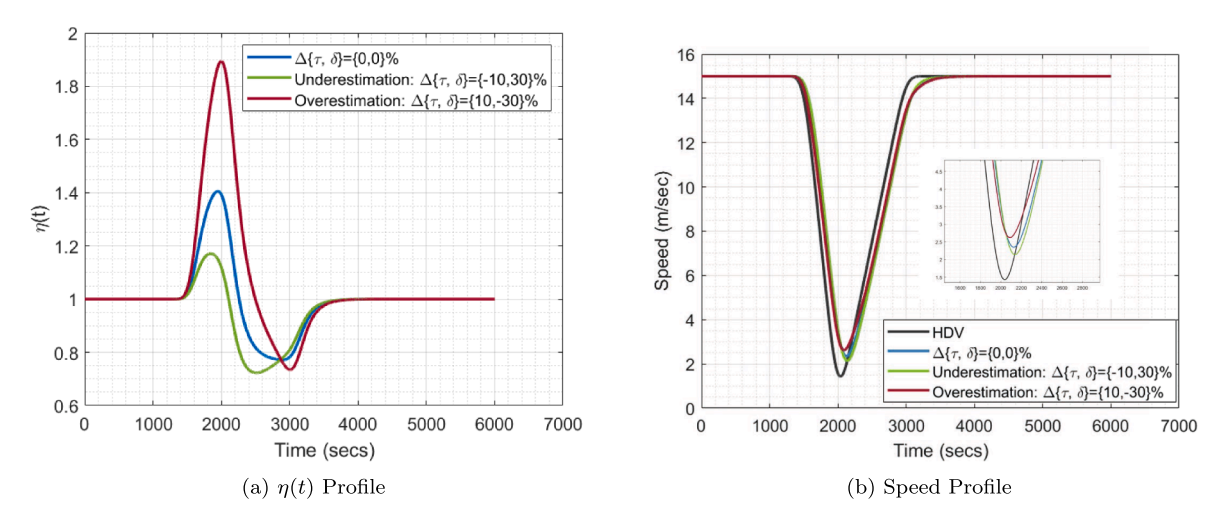


Fig. 18. The impacts of over/under estimation.

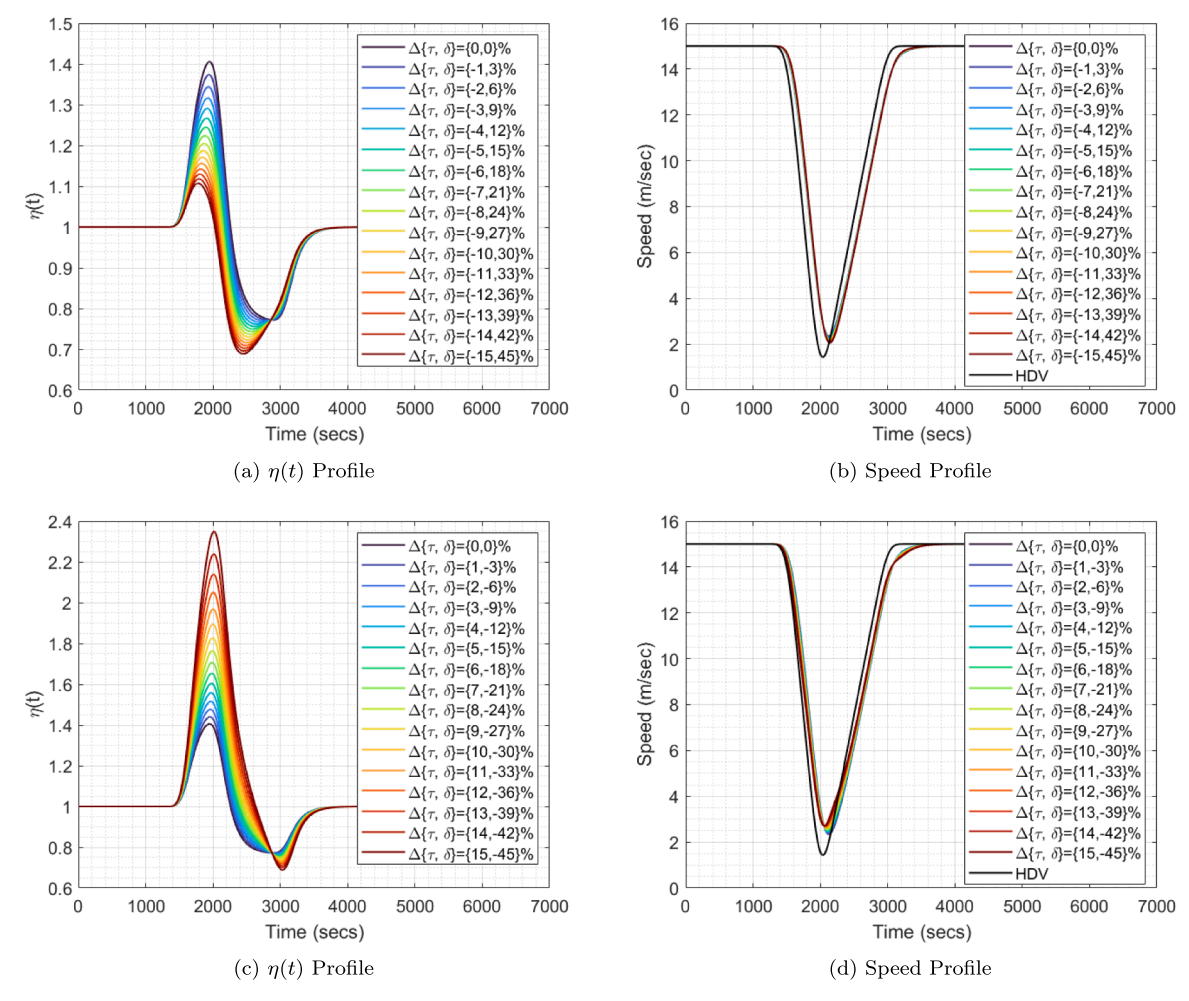


Fig. 19. Underestimation (top row); Overestimation (bottom row).

6.2. MPC Controller

Similar to the traffic impact study shown in Section 6.1, numerical simulations were run for platoons of MPC vehicles as well as mixed platoons of MPC and linear controller vehicles (see Fig. 17 for representative speed profiles). When MPC is unconstrained, the behavior is similar to that seen with linear controllers with equivalent control parameter settings (compare Figs. 17a and b). The more interesting scenario happens when constraints are introduced into the MPC vehicles. Fig. 17c shows the speed profile with a mixed platoon of linear controller and MPC vehicles where the MPC vehicles have limiting acceleration and deceleration constraints active. The constraints imposed are weak so that the MPC optimization algorithm is able to find feasible solutions. This however leads to the constraints becoming limiting only for the first MPC vehicle in the platoon (subsequent vehicles never reach constraint conditions). As can be seen in Fig. 17c, active constraints would result in an increase in the disturbance duration, possibly with a secondary disturbance being created.

Stronger imposed acceleration and deceleration constraints may become active for multiple vehicles in a platoon. This presents a very interesting scenario since platoon ordering and interactions between heterogeneous settings would become increasingly relevant in the presence of strongly constrained MPCs. Further, enough vehicles with active constraints in a platoon may lead to overall disturbance amplification, even if weight parameters are set for string stability when unbounded. A full investigation of traffic-level impacts of platoons of strongly constrained MPC, however, remains outside of the scope of the present work due to the high complexity of such an undertaking. Nonetheless, the mechanisms observed above provide insight into possible disturbance propagation through the platoon.

7. Conclusion

This paper aimed to unveil the physical CF behaviors of AVs under different vehicle control paradigms and settings, and cast light

on their traffic-level impacts. To this end, we developed a comprehensive analysis framework, consisting of (i) approximation of AV CF behavior using the AB model, (ii) mapping between control parameters and the AB model parameters through numerical simulations, and (iii) prediction of the AB model parameters given control parameters and lead vehicle trajectory using data-driven methods. Specifically, substantiated by empirical evidence, the AB model was adopted as a unifying framework to connect microscopic control mechanisms to more aggregate physical CF response to disturbances. The empirical analysis showed that the reaction pattern, $\eta(t)$, of the AB model can flexibly capture a wide range of CF behaviors possible under different control logic.

Building on this, we focused on analyzing two well-known controllers: linear state-feedback controller and MPC-based controller. Particularly, we analyzed a linear state-feedback controller to explore how different control gain settings influence the CF behavior. Three main results are notable: (i) three control gains guide the controller with different mechanisms, leading to different CF behaviors; (ii) the compound effect of control gains produces two prevalent $\eta(t)$ reaction patterns: convex-concave and concave-convex (weak concavity and weak convexity represent Newell-like behavior); and (iii) an intrinsic mapping relationship exists between the control gains and $\eta(t)$ parameters, casting light on implications for traffic dynamics.

A MPC-based controller was analyzed in a similar fashion. Particularly, we examined two cases pertaining to the constraints in the MPC-based controller: unbounded and bounded acceleration/deceleration. The analysis showed that in unbounded setting, MPC control mechanisms can be consistent with the linear controller, and similar $\eta(t)$ reaction patterns were observed. However, in bounded settings, deviations from these reaction patterns occur in the form of greater convexity (concavity) with bounded deceleration (acceleration). Moreover, constraints from deceleration and acceleration can interact. The compound effects can result in instability (in the form of a decrease in minimum speed), acceleration and speed overshooting during recovery, and prolonged recovery to the original state.

Building on the insights from the analysis, we formulated a data-driven approach to predict the reaction pattern, $\eta(t)$, based on control parameter setting and disturbance characteristics. The approach consists of (i) a logistic classifier to predict the $\eta(t)$ shape and (ii) a convoluted Multivariate Gaussian Process (MGP) to predict the η^{min} and η^{max} while addressing correlation between them. The models were validated using simulated AV data, as well as real AV data, which demonstrated promising performance.

Extending these results, we then analyzed disturbance evolution through a platoon of vehicles with multi-class AVs controlled through different gain settings. The simulations revealed that disturbance propagation for a platoon of heterogeneous vehicles is dependent on the dominant vehicle type, the aggregate impact on disturbance is an average of individual impacts of vehicle types involved, and that the platoon ordering does not have a significant impact on disturbance propagation. The simulation results also show that platoons with convex-concave dominant behavior lead to oscillation amplification and possible overshooting in speed leading to creation of a secondary disturbance and increasing the oscillation duration.

This study serves as an important step toward connecting microscopic AV control algorithms to macroscopic traffic wide impacts. The proposed analysis framework is general, such that it can be applied to a variety of controllers and better guide the AV control design or setting with the system-level performance in mind. Nevertheless, several directions for future research is desired. In this work, a knowledge of the controller is needed to directly explore the analysis framework developed. If the controller is unknown (e.g., due to propriety rights), but field data suggests that it could likely follow a known controller (e.g., linear controller), then we have shown in Sections 2.2 and 5.4 how we can calibrate needed parameters and follow the developed analysis framework (we also refer to relevant work by Chen et al. (2012a) on this matter). However, if no knowledge exists on the controller's structure, as seen in AI-based controllers, applying the proposed framework needs further research investigation. Additionally, this work focused only on a single stop-and-go disturbance and could be expanded to study the behavior under multiple interactive disturbances (i.e., oscillations). More research is needed to elucidate the traffic wide impacts under multiple controllers from different paradigms (e.g., AI-based control), constraint settings, and platoon compositions. Furthermore, incorporating connectivity (including communication delay) would also lead to a more general understanding of multi-class AV traffic. Another important direction would be to expand the MSP prediction model to predict the timings of η^{min} and η^{max} , which could affect disturbance propagation. While the same modeling framework can be adopted, the main challenges lies in addressing the functional covariance between (η^{min} , η^{max}) and their timings to obtain robust and accurate predictions. These are part of ongoing research by the authors.

Acknowledgement

This research was sponsored by the National Science Foundation through Awards CMMI 1932932, CMMI 1932921, and CMMI 1826162.

Appendix A. Appendix

In here we provide a sensitivity analysis with respect to parameters τ and δ when they need to be calibrated. We show the sensitivity analysis results for two representative cases; concave-convex reaction pattern (k = [3.0, 3.0, -1.2]), and convex-concave reaction pattern (k = 1.2, 1.2, -1.8). Note that δ and τ are inherently tied, and thus vary together. Specifically, the corresponding δ for a misestimated τ is calibrated using the steady state equilibrium CF for the follower. This suggests that over-estimation of τ leads to underestimation of δ (in order to produce same equilibrium conditions). Considering that δ (standstill spacing) is bounded by a vehicle's length, the relationship imposes a natural upper bound for over-estimation of τ . Furthermore, τ (time gap setting in the controller) is practically bounded through minimum safety considerations to avoid collision.

For the sensitivity analysis, we use a leader (HDV) trajectory and construct a follower's trajectory (given each of the control gain

Table 6Summary of sensitivity results: Concave-Convex.

$\Delta \tau (\%)$	$\Delta\delta(\%)$	$\Delta\eta^{min}(\%)$	$\Delta\eta^{max}(\%)$	$\Delta V_{drop}(\%)$	$\Delta \tau (\%)$	$\Delta\delta(\%)$	$\Delta\eta^{min}(\%)$	$\Delta\eta^{max}(\%)$	$\Delta V_{drop}(\%)$
-1.00	3.00	-0.03	-2.26	-0.16	1.00	-3.00	-0.14	2.43	0.23
-2.00	6.00	-0.19	-4.38	-0.35	2.00	-6.00	-0.37	5.03	0.44
-3.00	9.00	-0.66	-6.34	-0.52	3.00	-9.00	-0.66	7.83	0.65
-4.00	12.00	-1.30	-8.17	-0.71	4.00	-12.00	-1.04	10.84	0.86
-5.00	15.00	-2.03	-9.09	-0.88	5.00	-15.00	-1.48	14.08	1.08
-6.00	18.00	-2.83	-11.46	-1.05	6.00	-18.00	-1.99	17.57	1.31
-7.00	21.00	-3.66	-12.93	-1.21	7.00	-21.00	-2.57	21.35	1.53
-8.00	24.00	-4.53	-14.24	-1.36	8.00	-24.00	-3.22	25.44	1.75
-9.00	27.00	-5.41	-15.55	-1.51	9.00	-27.00	-4.00	29.89	1.96
-10.00	30.00	-6.30	-16.70	-1.66	10.00	-30.00	-4.80	34.72	2.17
-11.00	33.00	-7.20	-17.77	-1.80	11.00	-33.00	-5.73	40.02	2.36
-12.00	36.00	-8.09	-18.74	-1.93	12.00	-36.00	-6.77	45.82	2.52
-13.00	39.00	-8.98	-19.64	-2.06	13.00	-39.00	-7.94	52.20	2.68
-14.00	42.00	-9.86	-20.47	-2.19	14.00	-42.00	-9.26	59.26	2.78
-15.00	45.00	-10.73	-21.23	-2.32	15.00	-45.00	-10.74	67.10	2.84

settings mentioned above), with a known true τ and δ setting. This serves as the ground truth for the leader–follower pair trajectory. We then compute the estimated (with errors) $\eta(t)$ profile using; (i) the range of τ (and corresponding δ) values reflecting calibration error in parameters for the sensitivity testing, and (ii) the ground truth follower trajectory. Consequently, we use the estimated $\eta(t)$ profile to reconstruct a corresponding speed profile for the follower (i.e., AV).

The following are results of sensitivity analysis for the case of (i) concave-convex and (ii) convex-concave. We first present a closer look into the sensitivity of under/over estimation (considering a concave-convex pattern). We then extend and tabulate the results for both concave-convex and convex-concave patterns. Note: we will hereby refer to underestimation as the case where the estimated τ value is less than the true value (the opposite is true for overestimation).

Results from the sensitivity analysis (for both patterns) show that $\eta(t)$ profile is sensitive to variations in τ and δ ; however the reconstructed speed profile is more robust, with negligible variations. Fig. 18 provides a closer look into the impact of under and over estimation of τ (and accordingly δ) in green and red plot, respectively. Key insights are: (1) the overall shape of $\eta(t)$ remains consistent despite the changes in the values (this is also seen in the extended results in Fig. 19); (2) there is a shift (w.r.t time) in the overall $\eta(t)$ profile; (3) there are very small changes in the speed profile. Insights (1) and (2) combine together to create the overall robust speed profile. We also note that in underestimation the extent of distortion (in terms of magnitude) is less than the overestimation case. This is due to the fact than in overestimation the parameter δ is decreasing significantly and approaching 0, and thus will have greater impact as it is a denominator term in Eqn. (7).

We now shift our attention towards a physical implication of under/over estimation. In case of an underestimation (in a concave-convex reaction pattern), from the estimated speed profile, one will see a lower dampening ability (i.e., drop in speed) than the ground truth (see the lowest speed in the green plot vs. the blue plot in Fig. 1(b)). Additionally, a smaller undershoot (than the ground truth) in velocity (in the recovery phase) is observed. The opposite is true in case of overestimation. Further, we note that in case of overestimation the impact is slightly higher. This suggests that overestimation is not desirable and should be avoided if possible as one would reckon that performance is better than what it actually is. Fig. 2. presents more details on under/over estimations.

The Case of Concave-Convex:

Table 6 and Fig. 19, provide a summary of the extended results of the sensitivity analysis done for a concave-convex pattern.

Table 7Summary of sensitivity results: Convex-Concave.

$\Delta \tau (\%)$	$\Delta\delta(\%)$	$\Delta\eta^{min}(\%)$	$\Delta\eta^{max}(\%)$	$\Delta V_{drop}(\%)$	$\Delta au(\%)$	$\Delta\delta(\%)$	$\Delta \eta^{min}(\%)$	$\Delta\eta^{max}(\%)$	$\Delta V_{drop}(\%)$
-1.00	3.00	-2.33	-1.38	0.14	1.00	-3.00	2.47	1.49	0.04
-2.00	6.00	-4.52	-2.64	0.17	2.00	-6.00	5.09	3.20	-0.02
-3.00	9.00	-6.60	-3.80	0.22	3.00	-9.00	7.90	4.86	-0.08
-4.00	12.00	-8.57	-4.85	0.25	4.00	-12.00	10.83	6.74	-0.15
-5.00	15.00	-10.43	-5.49	0.28	5.00	-15.00	14.09	8.83	-0.22
-6.00	18.00	-12.20	-6.01	0.31	6.00	-18.00	17.52	11.07	-0.30
-7.00	21.00	-13.88	-6.54	0.34	7.00	-21.00	21.21	13.50	-0.40
-8.00	24.00	-15.48	-6.97	0.36	8.00	-24.00	25.18	16.16	-0.52
-9.00	27.00	-17.00	-7.40	0.39	9.00	-27.00	29.48	19.06	-0.63
-10.00	30.00	-18.46	-7.81	0.40	10.00	-30.00	34.15	22.23	-0.75
-11.00	33.00	-19.84	-8.20	0.42	11.00	-33.00	39.22	25.72	-0.90
-12.00	36.00	-21.17	-8.57	0.44	12.00	-36.00	44.78	29.55	-1.06
-13.00	39.00	-22.43	-8.92	0.45	13.00	-39.00	50.86	33.80	-1.25
-14.00	42.00	-23.65	-9.25	0.47	14.00	-42.00	57.57	38.51	-1.51
-15.00	45.00	-25.22	-10.27	0.52	15.00	-45.00	65.00	43.76	-1.72

The Case of Convex-Concave:

Note that the detailed impact of under/over estimation of τ and δ for a convex-concave pattern follows the same logic as the discussion provided for the above case. Table 7 presents the a summary of results into the sensitivity analysis for a convex-concave pattern.

References

- Allwein, E.L., Schapire, R.E., Singer, Y., 2000. Reducing multiclass to binary: A unifying approach for margin classifiers. J. Mach. Learn. Res. 1, 113–141. Alvarez, M., Lawrence, N.D., 2009. Sparse convolved gaussian processes for multi-output regression. Advances in neural information processing systems 57–64. Álvarez, M.A., Lawrence, N.D., 2011. Computationally efficient convolved multiple output gaussian processes. The Journal of Machine Learning Research 12, 1459–1500.
- Burt, D.R., Rasmussen, C.E., Van Der Wilk, M., 2019. Rates of convergence for sparse variational gaussian process regression. arXiv preprint arXiv:1903.03571. Chen, D., Ahn, S., Laval, J., Zheng, Z., 2014. On the periodicity of traffic oscillations and capacity drop: the role of driver characteristics. Transportation research part B: methodological 59, 117–136.
- Chen, D., Laval, J., Zheng, Z., Ahn, S., 2012a. A behavioral car-following model that captures traffic oscillations. Transportation research part B: methodological 46, 744–761.
- Chen, D., Laval, J.A., Ahn, S., Zheng, Z., 2012b. Microscopic traffic hysteresis in traffic oscillations: A behavioral perspective. Transportation Research Part B: Methodological 46, 1440–1453.
- Chen, D., Srivastava, A., Ahn, S., Li, T., 2019. Traffic dynamics under speed disturbance in mixed traffic with automated and non-automated vehicles. Transportation Research Part C: Emerging Technologies.
- Chen, N., Wang, M., Alkim, T., van Arem, B., 2018. A robust longitudinal control strategy of platoons under model uncertainties and time delays. Journal of Advanced Transportation 2018.
- Damianou, A.C., Titsias, M.K., Lawrence, N.D., 2016. Variational inference for latent variables and uncertain inputs in gaussian processes. The Journal of Machine Learning Research 17, 1425–1486.
- Darbha, S., Rajagopal, K., 1999. Intelligent cruise control systems and traffic flow stability. Transportation Research Part C: Emerging Technologies 7, 329–352. Dunbar, W.B., Caveney, D.S., 2011. Distributed receding horizon control of vehicle platoons: Stability and string stability. IEEE Trans. Autom. Control 57, 620–633. Gao, W., Jiang, Z.P., 2017. Nonlinear and adaptive suboptimal control of connected vehicles: A global adaptive dynamic programming approach. Journal of Intelligent & Robotic Systems 85, 597–611.
- Gao, W., Jiang, Z.P., Ozbay, K., 2016. Data-driven adaptive optimal control of connected vehicles. IEEE Trans. Intell. Transp. Syst. 18, 1122-1133.
- Gong, S., Du, L., 2018. Cooperative platoon control for a mixed traffic flow including human drive vehicles and connected and autonomous vehicles. Transportation research part B: methodological 116, 25–61.
- Gong, S., Shen, J., Du, L., 2016. Constrained optimization and distributed computation based car following control of a connected and autonomous vehicle platoon. Transportation Research Part B: Methodological 94, 314–334.
- Hoogendoorn, S., Hoogendoorn, R., Wang, M., Daamen, W., 2012. Modeling driver, driver support, and cooperative systems with dynamic optimal control. Transportation research record 2316, 20–30.
- Hou, Z., Xu, J.X., Zhong, H., 2007. Freeway traffic control using iterative learning control-based ramp metering and speed signaling. IEEE Transactions on vehicular technology 56, 466–477.
- Hou, Z.S., Wang, Z., 2013. From model-based control to data-driven control: Survey, classification and perspective. Inf. Sci. 235, 3–35.
- Kendall, A., Gal, Y., 2017. What uncertainties do we need in bayesian deep learning for computer vision? Advances in neural information processing systems
- Knoop, V., Hoogendoom, S., Adams, K., 2009. Capacity reductions at incidents sites on motorways. European Journal of Transport and Infrastructure Research 9. Kuderer, M., Gulati, S., Burgard, W., 2015. Learning driving styles for autonomous vehicles from demonstration. In: 2015 IEEE International Conference on Robotics and Automation (ICRA), pp. 2641–2646.
- Laval, J.A., Leclercq, L., 2010. A mechanism to describe the formation and propagation of stop-and-go waves in congested freeway traffic. Philosophical Transactions of the Royal Society A: Mathematical, Physical and Engineering Sciences 368, 4519–4541.
- Lefèvre, S., Carvalho, A., Borrelli, F., 2016. A learning-based framework for velocity control in autonomous driving. IEEE Trans. Autom. Sci. Eng. 13, 32–42.
- Li, T., Chen, D., Zhou, H., Laval, J., Xie, Y., 2021. Car-following behavior characteristics of adaptive cruise control vehicles based on empirical experiments. Transport. Res. Part B: Methodol. 147, 67–91. https://doi.org/10.1016/j.trb.2021.03.003.
- Liu, H., Kan, X.D., Shladover, S.E., Lu, X.Y., Ferlis, R.E., 2018. Modeling impacts of cooperative adaptive cruise control on mixed traffic flow in multi-lane freeway facilities. Transportation Research Part C: Emerging Technologies 95, 261–279.
- Liu, H., Ong, Y.S., Shen, X., Cai, J., 2020. When gaussian process meets big data: A review of scalable gps. In: IEEE Transactions on Neural Networks and Learning Systems.
- Ma, J., Li, X., Zhou, F., Hu, J., Park, B.B., 2017. Parsimonious shooting heuristic for trajectory design of connected automated traffic part ii: computational issues and optimization. Transportation Research Part B: Methodological 95, 421–441.
- Marsden, G., McDonald, M., Brackstone, M., 2001. Towards an understanding of adaptive cruise control. Transportation Research Part C: Emerging Technologies 9, 33–51.
- Milanés, V., Shladover, S.E., 2014. Modeling cooperative and autonomous adaptive cruise control dynamic responses using experimental data. Transportation Research Part C: Emerging Technologies 48, 285–300.
- Milanés, V., Shladover, S.E., Spring, J., Nowakowski, C., Kawazoe, H., Nakamura, M., 2013. Cooperative adaptive cruise control in real traffic situations. IEEE Transactions on intelligent transportation systems 15, 296–305.
- Montanino, M., Punzo, V., 2013. Making ngsim data usable for studies on traffic flow theory: Multistep method for vehicle trajectory reconstruction. Transp. Res. Rec. 2390, 99–111.
- Morbidi, F., Colaneri, P., Stanger, T., 2013. Decentralized optimal control of a car platoon with guaranteed string stability. In: 2013 European Control Conference (ECC), IEEE, pp. 3494–3499.
- Morbidi, F., Mariottini, G.L., 2012. Active target tracking and cooperative localization for teams of aerial vehicles. IEEE transactions on control systems technology 21, 1694–1707.
- Naus, G.J., Vugts, R.P., Ploeg, J., van De Molengraft, M.J., Steinbuch, M., 2010. String-stable cacc design and experimental validation: A frequency-domain approach. IEEE Transactions on vehicular technology 59, 4268–4279.
- Öncü, S., Ploeg, J., van de Wouw, N., Nijmeijer, H., 2014. Cooperative adaptive cruise control: Network-aware analysis of string stability. IEEE Trans. Intell. Transp. Syst. 15, 1527–1537.
- Newell, G.F., 2002. A simplified car-following theory: a lower order model. Transportation Research Part B: Methodological 36, 195–205.
- Öncü, S., Ploeg, J., Van de Wouw, N., Nijmeijer, H., 2014. Cooperative adaptive cruise control: Network-aware analysis of string stability. IEEE Trans. Intell. Transp. Syst. 15, 1527–1537.
- Ozdemir, A.A., Gumussoy, S., 2017. Transfer function estimation in system identification toolbox via vector fitting. IFAC-PapersOnLine 50, 6232-6237.

Peppard, L., 1974. String stability of relative-motion pid vehicle control systems. IEEE Trans. Autom. Control 19, 579–581.

Petrillo, A., Salvi, A., Santini, S., Valente, A.S., 2018. Adaptive multi-agents synchronization for collaborative driving of autonomous vehicles with multiple communication delays. Transportation research part C: emerging technologies 86, 372–392.

Phillips, J., Cripps, E., Lau, J.W., Hodkiewicz, M., 2015. Classifying machinery condition using oil samples and binary logistic regression. Mechanical Systems and Signal Processing 60, 316–325.

Qin, W.B., Orosz, G., 2017. Scalable stability analysis on large connected vehicle systems subject to stochastic communication delays. Transportation Research Part C: Emerging Technologies 83, 39–60.

Rasmussen, C.E., 2003. Gaussian processes in machine learning. Summer School on Machine Learning, Springer. 63-71.

Shladover, S.E., Nowakowski, C., Lu, X.Y., Ferlis, R., 2015. Cooperative adaptive cruise control: Definitions and operating concepts. Transp. Res. Rec. 2489, 145–152. Shladover, S.E., Su, D., Lu, X.Y., 2012. Impacts of cooperative adaptive cruise control on freeway traffic flow. Transp. Res. Rec. 2324, 63–70.

Snelson, E., Ghahramani, Z., 2006. Sparse gaussian processes using pseudo-inputs. Advances in neural information processing systems 1257–1264.

Stankovic, S.S., Stanojevic, M.J., Siljak, D.D., 2000. Decentralized overlapping control of a platoon of vehicles. IEEE Trans. Control Syst. Technol. 8, 816–832.

Stein, A., Corsten, L., 1991. Universal kriging and cokriging as a regression procedure. Biometrics 575-587.

Stein, M., 1987. Large sample properties of simulations using latin hypercube sampling. Technometrics 29, 143-151.

Stern, R.E., Cui, S., Delle Monache, M.L., Bhadani, R., Bunting, M., Churchill, M., Hamilton, N., Pohlmann, H., Wu, F., Piccoli, B., et al., 2018. Dissipation of stop-and-go waves via control of autonomous vehicles: Field experiments. Transportation Research Part C: Emerging Technologies 89, 205–221.

Swaroop, D., Hedrick, J.K., 1996. String stability of interconnected systems. IEEE transactions on automatic control 41, 349-357.

Swaroop, D., Hedrick, J.K., Chien, C., Ioannou, P., 1994. A comparision of spacing and headway control laws for automatically controlled vehicles1. Vehicle system dynamics 23, 597–625.

Talebpour, A., Mahmassani, H.S., 2016. Influence of connected and autonomous vehicles on traffic flow stability and throughput. Transportation Research Part C: Emerging Technologies 71, 143–163.

Talebpour, A., Mahmassani, H.S., Hamdar, S.H., 2011. Multiregime sequential risk-taking model of car-following behavior: specification, calibration, and sensitivity analysis. Transportation research record 2260, 60–66.

Van Arem, B., Van Driel, C.J., Visser, R., 2006. The impact of cooperative adaptive cruise control on traffic-flow characteristics. IEEE Transactions on intelligent transportation systems 7, 429–436.

VanderWerf, J., Shladover, S., Kourjanskaia, N., Miller, M., Krishnan, H., 2001. Modeling effects of driver control assistance systems on traffic. Transp. Res. Rec. 1748, 167–174.

Wang, M., 2018. Infrastructure assisted adaptive driving to stabilise heterogeneous vehicle strings. Transportation Research Part C: Emerging Technologies 91, 276–295

Wang, M., Daamen, W., Hoogendoorn, S.P., van Arem, B., 2014. Rolling horizon control framework for driver assistance systems. part i: Mathematical formulation and non-cooperative systems. Transportation research part C: emerging technologies 40, 271–289.

Wu, C., Kreidieh, A., Parvate, K., Vinitsky, E., Bayen, A.M., 2017. Flow: Architecture and benchmarking for reinforcement learning in traffic control. arXiv preprint arXiv:1710.05465. 10.

Yi, K., Do Kwon, Y., 2001. Vehicle-to-vehicle distance and speed control using an electronic-vacuum booster. JSAE review 22, 403-412.

Zhao, J., Sun, S., 2016. Variational dependent multi-output gaussian process dynamical systems. The Journal of Machine Learning Research 17, 4134–4169. Zhou, M., Qu, X., Li, X., 2017a. A recurrent neural network based microscopic car following model to predict traffic oscillation. Transportation research part C: emerging technologies 84, 245–264.

Zhou, Y., Ahn, S., 2019. Robust local and string stability for a decentralized car following control strategy for connected automated vehicles. Transportation Research Part B: Methodological 125, 175–196.

Zhou, Y., Ahn, S., Chitturi, M., Noyce, D.A., 2017b. Rolling horizon stochastic optimal control strategy for acc and cacc under uncertainty. Transportation Research Part C: Emerging Technologies 83, 61–76.

Zhou, Y., Ahn, S., Wang, M., Hoogendoorn, S., 2020. Stabilizing mixed vehicular platoons with connected automated vehicles: An h-infinity approach. Transportation Research Part B: Methodological 132, 152–170.

Zhou, Y., Wang, M., Ahn, S., 2019. Distributed model predictive control approach for cooperative car-following with guaranteed local and string stability. Transportation research part B: methodological 128, 69–86.